THE ASTROPHYSICAL JOURNAL, 373:633–648, 1991 June 1

BOWEN FLUORESCENCE IN AM HERCULIS STARS[1]

JONATHAN SCHACHTER,[2,3] ALEXEI V. FILIPPENKO,[4,5] STEVEN M. KAHN,[2,6,7] AND FRITS B. S. PAERELS[2,7,8]
University of California, Berkeley
Received 1990 July 13; accepted 1990 November 19

ABSTRACT

We relate new observations of Bowen fluorescence lines in AM Her and EF Eri, two AM Her systems. These objects display a rich array of Bowen lines, including O III $\lambda\lambda$3123, 3133, 3299, 3312, 3341, 3407, 3429, 3444 and N III $\lambda\lambda$4634, 4641, 4642. There is unambiguous evidence for the O3 process in the cascades of O III. We also see strong emission lines of H I, He I, and He II, together with a few detections of Ca II and C II. Many of these lines show a complex multiple-component structure, which differs significantly from that observed by previous investigators.

The intensity ratios of H I, He I, and He II emission line series depart from those expected in case B recombination. For our H I and He II observations of AM Her and EF Eri, the line ratios are much flatter than case B, suggesting substantial line opacities. We use a simple thin slab model to calculate constraints on the expected optical depths and electron temperatures in the H I zone and (for AM Her) in the He II zone. In AM Her, allowed opacity and temperature values are strongly correlated. However, in this object we invariably find $T \gtrsim 7000$ K and $\tau_{\mathrm{H}\alpha} \gtrsim 100$ in the H I zone, whereas $T \gtrsim 20{,}000$ K and $\tau_{1640} \lesssim 200$ in the He II zone. The analysis yields $\tau_{\mathrm{H}\alpha} \approx 200$ for EF Eri. By making the assumption that the He II level populations approach LTE, we can use the observed Bowen line intensities to estimate the size (R), density, and temperature of the emission region. We find $R \approx 10^8$–10^9 cm, $n_e \approx 10^{11}$–10^{18} cm^{-3}, and $T_e \approx 20{,}000$–$30{,}000$ K. The derived values of R are significantly less than the size of the Roche lobe of the white dwarf [$\sim$(2–5) $\times$ 10^{10} cm]; hence, we may be probing a length scale in the accretion column. The large range of densities reflects the exponential temperature dependence in our expression for n_e, so that better temperature estimates from future observations will produce tighter n_e constraints.

Subject headings: atomic processes — radiative transfer — stars: binaries — stars: emission-line — stars: individual (AM Herculis, EF Eridani) — ultraviolet: spectra

1. INTRODUCTION

This is the third paper in a series on Bowen fluorescence in compact X-ray sources. In the first work (Schachter, Filippenko, & Kahn 1989, hereafter Paper I), we studied Bowen fluorescence (BF) in the Scorpius X-1 binary system, while in the second we discussed BF in a sample of eight Seyfert 2 and narrow-line Seyfert 1 nuclei (Schachter, Filippenko, & Kahn 1990, hereafter Paper II). Many of these sources show strong O III $\lambda\lambda$3133, 3444 Bowen emission—predicted to be the strongest observed transitions by atomic physics calculations (Saraph & Seaton 1980, hereafter SS). These O III lines are radiative cascades produced by the trapping of He II Lyα (λ303.783), which is nearly resonant with a ground-state O III transition ($2p3d \rightarrow 2p^2$; Bowen 1934). In Figure 1, we provide a Grotrian diagram of important oxygen Bowen cascades. A similar coincidence of wavelengths between one of the extreme ultraviolet (UV) O III Bowen cascades and N III produces the nitrogen Bowen lines, $\lambda\lambda$4634, 4641, 4642. See Figure 1 of Paper I for a Grotrian diagram with details of the N III cascades.

As demonstrated in our earlier work, simple models of the emission-line regions (ELRs) of accretion-powered sources can be inferred from Bowen observations, even over a dramatically large range of source sizes, densities, and geometries. In the present paper, we extend our analysis to include AM Her systems, in which BF can be used to study accretion in a highly nonspherical geometry, complicated by strong magnetic fields. Optical spectroscopic studies of these systems reveal a rich emission-line spectrum, including strong H I Balmer lines, He I, and He II (see Cropper 1988 for a review). Because of the difficulty of performing ground-based observations at wavelengths near the atmospheric limit, AM Her objects have been largely unobserved in the spectral region $\sim$3100–3400 Å. The one notable exception is AM Her itself, in which Raymond et al. (1979) reported detecting the O III $\lambda\lambda$3123, 3133 Bowen lines in a long-wavelength *International Ultraviolet Explorer* (*IUE*) spectrum. The quoted intensity of these Bowen lines is relatively uncertain, as they were apparently only marginally detected (Raymond 1989). In Galactic X-ray binaries, the nitrogen Bowen lines appear as a broad feature, with possible additional contributions from C III and O II, centered near 4640 Å, (e.g., McClintock, Canizares, & Tarter 1975). The 4640 Å feature, often partly blended with He II λ4686, is commonly seen in AM Her systems, including AM Her itself (Stockman et al. 1977, hereafter S77), VV Pup (Schneider & Young 1980), EF Eri (Young et al. 1982), QQ Vul (= E2003+225; McCarthy, Bowyer, & Clarke 1986), PG1550+191 (Schmidt, Stockman,

[1] Based on observations made at Lick Observatory, which is owned and operated by the University of California.
[2] Department of Physics and Space Sciences Laboratory.
[3] Postal address: Harvard-Smithsonian Center for Astrophysics, 60 Garden Street, Cambridge, MA 02138.
[4] Postal address: Department of Astronomy, University of California, Berkeley, CA 94720.
[5] Presidential Young Investigator.
[6] Also affiliated with Laboratory for Experimental Astrophysics at Lawrence Livermore National Laboratory.
[7] Postal address: Department of Physics, University of California, Berkeley, CA 94720.
[8] Also affiliated with Institute of Geophysics and Planetary Physics at Lawrence Livermore National Laboratory.

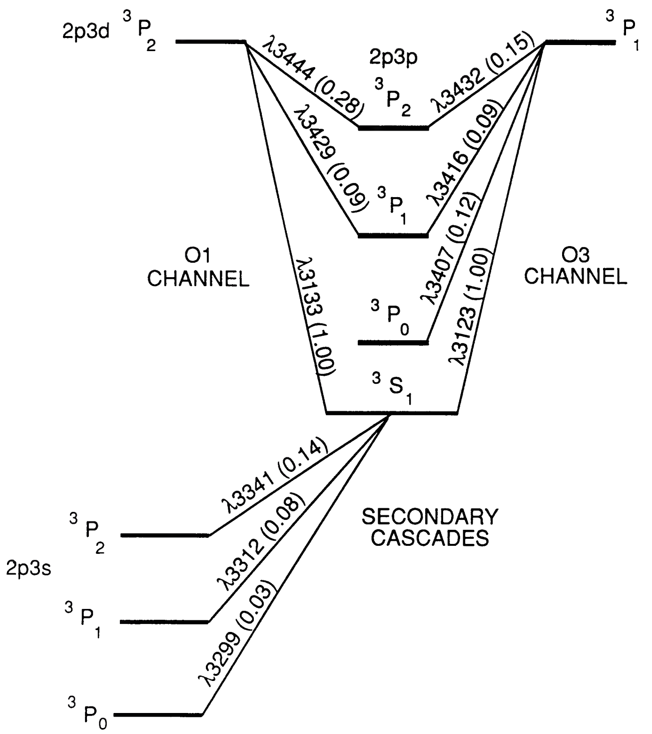

FIG. 1.—Grotrian diagram of O III Bowen lines. Indicated are important primary cascades for the O1 and O3 channels. Predicted cascade intensities are given relative to I_{3133} for the O1 channel, and relative to I_{3123} for the O3 channel. Resulting transitions (secondary cascades) are also shown, with intensities relative to I_{3133} or I_{3123}.

& Grandi 1986), and V834 Cen (= E1405−451; Rosen, Mason, & Córdova 1987). These objects constitute some 40% of the confirmed AM Her systems. Green et al. (1982) reported the 4640 Å blend in seven cataclysmic variable candidates from the Palomar Green survey; some of these objects may be AM Her stars as well.

In spite of the large number of AM Her systems with reported detections of the 4640 Å feature, direct evidence for BF can be provided only by the oxygen Bowen lines, since mechanisms such as the Of star process (dielectronic recombination of N IV) can produce the 4640 Å feature independently of BF (see § III*b* of Kastner & Bhatia 1990). The O III cascades also yield important ELR constraints, as discussed above. To quantify the relative importance of BF, we have performed a detailed study of two well-known, bright AM Her objects—AM Her and EF Eri—using the 3 m Shane reflector at Lick Observatory. We find that, together, AM Her and EF Eri possess eight oxygen Bowen lines: O III $\lambda\lambda$3123, 3133, 3299, 3312, 3341, 3407, 3429, 3444. The richness of the Bowen emission was completely unexpected, given that we had direct evidence only for $\lambda\lambda$3133, 3444 in Sco X-1 and in the Seyfert sample.

After a brief review of the observational difficulties inherent in our work, and the checks we perform to verify the accuracy of the data (§ 2), we describe the new data on AM Her and EF Eri (§ 3). The observed line ratios for H I and He II are shown to deviate significantly from those expected by case B recombination. In this light, we undertake a detailed study of the H I and He II emission in AM Her. This approach enables us to put limits on line and continuum optical depths, as well as temperatures (§ 4). We then use these limits and the observed Bowen emission to construct a simple picture of the ELRs in the two sources (§ 5).

2. OBSERVATIONS

2.1. *General*

All measurements were performed with the UV Schmidt system (Miller & Stone 1987) at the Cassegrain focus of the 3 m Shane reflector at Lick Observatory. We selected the two most luminous of known AM Her systems, AM Her itself ($V \approx 12$–14 mag) and EF Eri ($V \approx 13$–15 mag). Observing techniques were largely as discussed in Papers I and II. Stratospheric ozone absorption bands, which contaminate the spectrum shortward of ~ 3400 Å, were removed via division of the object spectrum by that of a hot DA white dwarf. We found that EG 139 (DA3), observed at air mass 1.0, was more effective in removing ozone than EG 162 (DA4), observed at air mass 1.8. This was true for observations of both AM Her (observed at air mass 1.1–1.5) and EF Eri (observed at air mass 2.0), and it therefore suggests that at the hotter photospheric temperature of EG 139 ($T \approx 16{,}800$ K, vs. $T \approx 12{,}600$ K for EG 162), the near-UV spectrum provides a cleaner continuum template.

Many of the data analysis procedures discussed in Paper II were needed specifically because the Seyfert nuclei are extended sources and have spectra contaminated by host galaxy starlight. Because the AM Her stars are unresolved, we extracted 3".2 slit spectra simply via a synthetic rectangular aperture of size 3".2 × 7".4, where 7".4 represents a sum of 11 CCD columns. Wide apertures (8") were used to check our flux calibration of AM Her. We found that the narrow-slit fluxes were smaller by $\lesssim 14\%$ at the blue wavelengths, with slightly better results at the green (8%) settings. Names and wavelength ranges of grating settings are indicated in Table 1. From a comparison of standard star spectra obtained on 1988 September 14, we estimate that EF Eri has flux calibration accurate to $\sim 10\%$.

2.2. *Implications of Source Variability*

Previous work on AM Her has suggested that emission-line ratios may vary significantly with binary phase ϕ (S77; Crampton & Cowley 1977). We use the usual magnetic-phase convention for the ephemeris (e.g., Young & Schneider 1979). Also, the continuum in AM Her from the optical to the hard X-ray band is observed to exhibit changes on time scales as short as tens of seconds (e.g., Tuohy et al. 1981). Since our measurements in different grating settings are taken at different times, intrinsic spectral variability could lead us to infer incorrect line ratios. At the outset of our study, we therefore performed a series of preliminary tests on the spectrum of AM Her, in order to quantify the importance of the technical problems associated with variability. We obtained a series of exploratory spectra of AM Her (not presented in this work) on 1988 July 16. Our first test was to study spectral variations between the UV and blue grating settings over a time corresponding to a phase change of $\Delta\phi = 0.10$. Note that $\Delta\phi = 0.10$ corresponds to ~ 1100 s for AM Her, whose orbital period is 3.09 hr. In a first look at the data, we found that emission lines common to the two bluest settings (H8–H10) show significant differences in both line shape and flux, differing in the latter by factors of up to 1.3. This discrepancy may represent changes in the source. As a second test, we compared two different UV spectra from the same night, separated by $\Delta\phi = 0.33$, and found dramatically different line shapes. Further tests on the 1988 July 16 data appear to indicate that for separations between settings given by $\Delta\phi \lesssim 0.04$, line shapes and fluxes do not vary appreciably ($\lesssim 10\%$).

We therefore used exposures corresponding to $\Delta\phi = 0.01$–0.04 and separations between settings in the range $\Delta\phi = 0.02$–0.05. These time scales are somewhat longer than the He II recombination time scale (for the derived electron density; § 5), $\sim 10^{-5}$ to 100 s, a quantity which reflects the mean time for the Bowen ELR to adjust to changes in the photoionizing continuum. However, the expected change in the soft X-ray luminosity seen by Tuohy et al. is $\lesssim 30\%$, when binned on time scales corresponding to our exposures. In our own spectra, line fluxes in the overlap between adjacent settings agree to $\sim 10\%$, except for the 1988 July 18 10:18 observation ($\lesssim 50\%$). The continua in the overlap regions agree very well, except for a constant scaling factor that presumably reflects small changes in atmospheric transparency and seeing.

We also determined that the observed spectrum of AM Her is relatively stable over periods of days to months. First, the observed continuum appears to be consistent in shape over the orbital period. Second, we find reasonable agreement between line flux measurements taken at different phases on successive observing nights. Fluxes of strong observed lines vary by $\lesssim 33\%$ in the 1988 July data, and by $\lesssim 25\%$ in the 1988 September data. Finally, comparing line fluxes in the July data to those of the September data reveals reasonable consistency.

Table 1 gives a summary of our observations of AM Her, with exposure times for individual grating settings. In the table, we introduce a shorthand notation to simplify discussion of the different sets of spectra: j1–j4 for the July observations, and s1–s7 for the September spectra. The j1 (1988 July 17) data for AM Her provide spectral coverage over nearly the entire wavelength band observable from the ground ($\sim$3100–9800 Å), with small differences in phase between adjacent settings. In order to isolate orbital variability of the Bowen lines and He II $\lambda\lambda$3204, 4686, we reobserved AM Her on 1988 July 18 with the UV, blue, and green settings at three equally spaced phase points around a single orbit (j2, j3, j4). On 1988 September 14, we obtained spectra with very short exposures using the UV setting only, at seven equally spaced phases around one orbit (s1–s7). This step was performed in order to study the Bowen line variability in greater detail.

For AM Her, data coming from the individual grating settings of 1988 July 17 were co-added to produce a single spectrum. We also assembled the separate settings of 1988 July 18 into three UV–green spectra.

The observed optical spectrum of EF Eri has also been previously reported to show variations (Schneider & Young 1980) over its orbital period of 81 minutes. The soft X-ray continuum of EF Eri is known to show variations on short time scales, with a prominent eclipse near $\phi = 0.44$ (Patterson, Williams, & Hiltner 1981), where we use the ephemeris from White (1981). Over the binary phase range of our observations, the soft X-ray continuum would be expected to vary by a factor of 1.5 to 2 outside of eclipse. Clearly, the large intrinsic variability in this object may affect observed line ratios.

EF Eri is too faint and too far south ($\delta_{1950} \approx -27°$) to perform the sort of exploratory variability tests we carried out for AM Her. Thus, the spectral and orbital coverage (Table 1) is more limited than for AM Her. The faint UV spectrum makes removal of stratospheric ozone absorption bands more difficult as well. Long exposures of EF Eri were needed for the required sensitivity in the near-UV. The continuum slopes are in relatively poor agreement between the two bluest settings. Line shapes are relatively Gaussian at the UV setting, but blue-peaked at the blue setting. For EF Eri, we co-added the UV–green observations. Small shifts (typically 15%–20%) were needed to match the continuum intensity between one setting and the adjacent one. The He I λ4471 line, which is in the overlap of the blue and green settings, is apparently redshifted by $\sim$200 km s^{-1} in the green setting relative to the blue one. A similar velocity shift was seen by Schneider & Young (1980) for the given change in ϕ. However, in view of the technical difficulties of producing consistent wavelength calibration from setting to setting (see Paper I), we cannot rule out that $\sim$50% of the observed wavelength shift between the two settings is merely an artifact. Given these considerations, a single spectrum based on the coaddition of our several observations of EF Eri can be viewed as representative only. Nevertheless, the detection of BF in this source is clear.

TABLE 1

OBSERVATION LOG[a]

Notation	Midpoint Time (1988 UT)	Setting	Midpoint ϕ	Exposure (s)
	AM Herculis			
j1	Jul 17 9:01	Green	0.55	150
	Jul 17 9:05	Blue	0.57	200
	Jul 17 9:11	UV	0.60	400
	Jul 17 9:20	Orange	0.66	100
	Jul 17 9:22	Red	0.65	150
	Jul 17 9:29	IR	0.70	200
j2	Jul 18 9:08	UV	0.34	400
	Jul 18 9:14	Blue	0.37	200
	Jul 18 9:18	Green	0.39	150
j3	Jul 18 10:12	UV	0.69	400
	Jul 18 10:18	Blue	0.71	200
	Jul 18 10:22	Green	0.74	150
j4	Jul 18 11:17	UV	0.04	400
	Jul 18 11:25	Blue	0.07	200
	Jul 18 11:28	Green	0.09	100
s1	Sep 14 4:13	UV	0.92	500
s2	Sep 14 4:43	UV	0.08	600
s3	Sep 14 5:12	UV	0.24	500
s4	Sep 14 5:49	UV	0.44	500
s5	Sep 14 6:17	UV	0.59	500
s6	Sep 14 6:49	UV	0.76	500
s7	Sep 14 7:19	UV	0.92	500
	EF Eridani			
	Sep 14 12:16	UV	0.14	1800
... .	Sep 14 12:39	Blue	0.42	600
	Sep 14 12:49	Green	0.54	300

[a] Approximate ranges of grating settings—UV: 3100–3900 Å; blue: 3750–4550 Å; green: 4400–5200 Å; orange: 4700–6300 Å; red: 5950–7550 Å; IR: 6600–9800 Å. Further details can be found in Table 1 of Paper I and § II*b* of Paper II. Ephemerides described in text. Magnetic phase convention used for AM Her.

3. NEW RESULTS

3.1. *AM Herculis*

The complete co-added spectrum of AM Her from j1 (notation as in Table 1) is presented in Figure 2. The strongest line is Hα. Especially notable are the strong Balmer discontinuity and flat Balmer decrement. Paschen-continuum emission and prominent high-order Paschen lines are evident. In Figure 3, we present the detailed j1 spectrum in segments of $\sim$1000 Å each. The spectrum is dominated by emission lines of H I, and He II, together with smaller contributions from other species, including Ca II and the O III Bowen lines. Tables 2 and 3

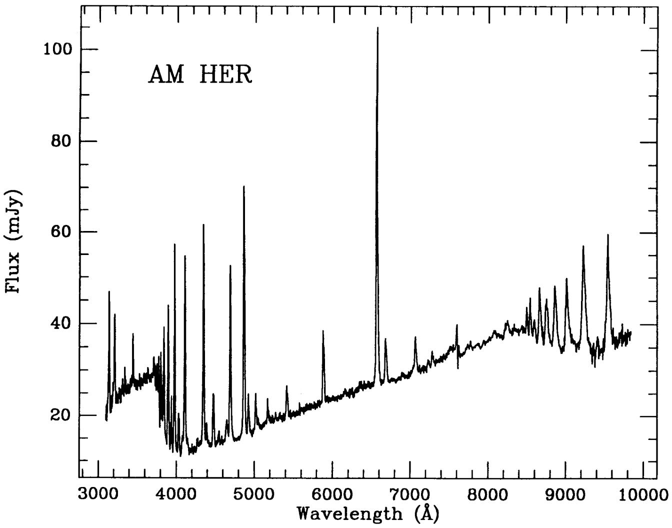

FIG. 2.—Complete spectrum of AM Her from the near-UV to the near-IR from 1988 July 17 data.

provide line fluxes for the 1988 July and 1988 September data. Our evidence for orbital variability in AM Her is presented in Figures 4 and 5. Figure 4, which compares four different observations of the UV–green region, provides an indication of a changing multicomponent structure in the observed emission lines (e.g., He II λ4686). This behavior is echoed in the high-order Balmer series, as seen in the comparison of seven UV spectra taken on 1988 September 14 (Fig. 5). A more complete discussion of the observed spectral lines is deferred to the specific subsections below.

3.1.1. *Bowen Lines*

In AM Her, our spectra provide clear evidence for a large number of O III BF lines, which are summarized in a Grotrian diagram (Fig. 1). The strong λλ3133, 3444 lines are clearly detected (Fig. 3*a*). The Bowen line profiles are similar to those of the high-order Balmer lines. Shortward of the Balmer discontinuity (3647 Å), the line spectrum of AM Her is completely dominated by light from BF lines and He II λ3204, The λλ3133, 3444 lines make a significant contribution to the entire spectrum (Fig. 2). Up to *eight* BF lines are seen. The clearest evi-

TABLE 2

AM HER EMISSION-LINE INTENSITIES IN 1988 JULY DATA[a]

Species	λ	$f_\nu(\lambda)$: j1[b]	$f_\nu(\lambda)$: j2	$f_\nu(\lambda)$: j3	$f_\nu(\lambda)$: j[4]
O III	3123	(blend ↓)	0168	(blend ↓)	0.250
O III	3133	0.955b	0.708	0.792b	0.779
He I	3188	0.189	0.171	0.132	0.193
He II	3204	0.867	0.726	0.556	0.900
Ne II	3267b[c]	...	...	...	0.086
O III	3299	(blend ↓)	0.027:	(blend ↓)	0.041:
O III	3312	0.176b	0.074	0.107b	0.087
O III	3341	0.218	0.185	0.133	0.200
O III	3407	(blend ↓)	...	...	0.098b[d]
O III	3429	(blend ↓)	0.070	0.042:	0.075
O III	3444	0.563b	0.250	0.238	0.244
He I	3587	0.093	0.065	0.051	0.047
He I	3614	0.082	...	...	...
He I	3634	0.094	0.078	0.049:	0.071
H16 + H15	3704	>0.081	>0.162	>0.098	(blend ↓)
H14	3722	>0.042	>0.083	>0.058	(blend ↓)
H13	3734	>0.075	>0.196	(blend ↓)	>0.490b
H12	3750	>0.123b[e]	(blend ↓)	(blend ↓)	(blend ↓)
H11	3771	>0.148	>0.889b	>0.749b	>0.817b
H10	3798	(blend ↓)	>0.618	(blend ↓)	>0.614
H9	3835	>1.152b[f]	>0.952b[f]	>1.089b[f]	>0.996b[f]
H8	3889	>0.828	>1.002	>0.683	>1.062
Ca II	3933	0.138	0.249	0.186	0.184
Hϵ	3970	1.152b[g]	1.278	0.976	1.418
He I	4026	0.266	0.323	0.257	0.333
O III + C III	4071	...	0.153	...	(blend ↓)
Hδ	4102	1.383:	1.450	1.172	1.932b
He I	4144	...	...	...	0.059
C II	4267	0.094:	0.078	0.072:	0.073
Hγ	4341	1.459b	1.520	1.194	1.715
He I	4388	(blend ↑)	0.122	0.123	0.114
He I	4471	0.403	0.407	0.352	0.400
He II	4542	0.084	0.075	0.081	0.074
N III	4640b[h]	0.176:	0.170	0.185	0.199
He II	4686	0.997b	0.960	0.912b	1.254
He I	4713	(blend ↑)	0.078	(blend ↑)	0.087
Hβ	4861	1.366b	1.500	1.271	1.643
He I	4922	0.195	0.185	0.197	0.194
He I	5016	0.180	0.171	0.251b	0.176
He I	5048	0.063:	0.052:	(blend ↑)	0.053
Fe I	5172	0.141	0.049	0.070	0.039
C III	5273	0.032	...	...	...
He II	5411	0.158	...	...	...
He I	5876	0.313	...	...	...
Si II	6360b[i]	0.028	...	...	...
Hα	6563	1.127	...	...	...
He I	6678	0.166	...	...	...
He I	7065	0.163	...	...	...
C II	7234b[j]	0.017	...	...	...
He I	7281	0.034	...	...	...
Ca II	8229b[k]	0.072	...	...	...
P16	8502	>0.058:	...	...	...
P15	8545	>0.077:	...	...	...
P14	8598	>0.047	...	...	...
P13	8665	>0.141	...	...	...
P12	8750	>0.146	...	...	...
P11	8863	>0.208	...	...	...
P10	9015	>0.275	...	...	...
P9	9229	>0.455	...	...	...
P8	9546	>0.473:	...	...	...

[a] Intensities in units of 10^{-12} ergs cm^{-2} s^{-1}; not dereddened. Wavelengths in Å. Notation "(blend)" indicates that given line is blended with one or more lines in same spectrum, and an arrow (↑ or ↓) is used to show the major blend contributor in the same column. The total intensity of the blend is listed followed by "b," under the entry for this strongest blend component. Lower limit values are for lines where continuum is contaminated by Stark-broadened H I lines, both Paschen and Balmer.

[b] Observation night designations as in Table 1.

[c] Blend of Ne II λλ3263, 3270.

[d] May be blended with O III λ3416 and O IV λλ3409, 3411, 3413.

[e] May be blended with He I λ3756.

[f] May be blended with He I λ3820.

[g] May contain contribution from Ca II λ3968.

[h] Probably also contains a contribution from C III and O II (see text).

[i] Blend of Si II λλ6347, 6371.

[j] Blend of C II λλ7231, 7236, 7237.

[k] Blend of Ca II λλ8202, 8249, 8255.

TABLE 3

AM HER EMISSION-LINE INTENSITIES IN 1988 SEPTEMBER DATA[a]

Ion	λ	s1[b]	s2	s3	s4	s5	s6	s7
O III	3123	0.124:	0.134:	0.200:	0.217:	0.192:	0.156:	0.249:
O III	3133	0.639	0.861	0.708	0.658	0.738	0.633	0.913
He I	3188	0.112	0.168	0.236	0.257	0.198	0.140	0.196
He II	3204	0.618	0.833	0.753	0.766	0.738	0.685	0.794
Ne II	3267b[c]	...	0.074	...	0.080	0.058:	0.060:	...
O III	3299	...	...	0.044	0.042	0.036	0.018:	...
O III	3312	0.058	0.076	0.105	0.101	0.092	0.081	0.098
O III	3341	0.125	0.174	0.171	0.174	0.200	0.167	0.178
O III	3407[d]	(blend ↓)	(blend ↓)	(blend ↓)	0.093	0.100	0.109	(blend ↓)
O III	3429	(blend ↓)	(blend ↓)	(blend ↓)	0.074	0.070	0.076	(blend ↓)
O III	3444	0.385b	0.469b	0.400b	0.238	0.245	0.231	0.438b
He I	3513	...	...	...	0.022	0.034:	0.022	...
He I	3530	0.028:	...	0.023:	0.021	0.036:	0.018	...
He I	3554	...	...	0.034:	0.030	0.033	0.027	0.034:
He I	3587[e]	0.057	0.087	0.072	0.057	0.067	0.068	0.062
He I	3614	0.041	0.052	0.054	0.045	0.043	0.044	0.051
He I	3634	0.041	0.084	0.076	0.060	0.050	0.060	0.085
H16 + H15	3704	>0.094	>0.141	>0.129	>0.136	>0.096	>0.129	(blend ↓)
H14	3722	>0.068	>0.083	>0.066	>0.073	>0.081	>0.055	>0.181b
H13	3734	>0.115	>0.122	>0.124	>0.142	>0.190	>0.129	>0.099
H12 + H13	3742[f]	>0.439b	>0.606b	>0.607b	>0.643b	>0.754b	>0.509b	>0.538b
H10	3798	>0.380	>0.512	>0.491	>0.527	>0.590	>0.474	>0.395
He I	3820	>0.095:	>0.106:	>0.171	>0.183	>0.170:	>0.128:	>0.132:
H9	3835	>0.594	>0.795	>0.642	>0.660	>0.723	>0.619	>0.705
H8	3889	0.696	0.897	0.782	0.871	0.951	0.751	0.789

[a] Intensities in units of 10^{-12} ergs cm^{-2} s^{-1}; not dereddened. Wavelengths in Å. Notation for blends as in Table 2. Lower limit values are for lines where continuum is contaminated by Stark-broadened Balmer lines.

[b] Observation night designations as in Table 1.

[c] Blend of Ne II $\lambda\lambda$3263, 3270.

[d] May be blended with O III λ3416 and O IV $\lambda\lambda$3409, 3411, 3413.

[e] Slight blending with $\lambda\lambda$3614, 3634.

[f] May be blended with O III λ3760.

dence for this is provided in Figure 5*e*, where we detect O III $\lambda\lambda$3123, 3133, 3299, 3312, 3341, 3407, 3429, 3444. The Bowen features appear to persist around the orbit, although sometimes velocity broadening produces line blends, for example λ3123 + λ3133 in Figure 5*a*. Blending also accounts for the complex structure observed in the feature near 3440 Å, which is probably a composite (λ3407 + λ3429 + λ3444). Determining the observed intensities of the blended lines is difficult (particularly for λ3444). Separation of the individual blended components into a sum of Gaussians is not possible. Instead, for these and other blended lines, we attempted to approximate the blended components visually. We estimate typical line flux uncertainties of 30% resulting from this method, although we note specific cases where the expected uncertainty could be significantly larger ($\lesssim$40%).

The *primary* ($2p3d \rightarrow 2p3p$) Bowen lines observed in our data can be divided into O1 and O3 process cascades. For secondary cascades ($2p3p \rightarrow 2p3s$; see below), this distinction vanishes. The O1 Bowen cascades come from the $2p3d\,^3P_2^o$ sublevel, whereas the O3 cascades arise in the $2p3d\,^3P_1^o$ sublevel. Both O1 and O3 transitions are present in our observations of AM Her. We begin by discussing the observed O1 cascades. The most intense observed Bowen line is λ3133, predicted to be the strongest O1 cascade (SS). Second in intensity in our observations is λ3444, for which atomic physics calculations predict $I_{3444}/I_{3133} = 0.28$. The clearest detections of λ3444 are j2, j3, j4 (Figs. 4*b*, 4*c*, and 4*d*) and s4, s5, s6 (Figs. 5*d*, 5*e*, and 5*f*). We find a mean value of $I_{3444}/I_{3133} \approx 0.34$, slightly larger than the predicted value.

After λ3444, the next strongest predicted O1 cascade is λ3429, where the calculated ratio is $I_{3429}/I_{3133} \approx 0.093$. The λ3429 line is seen most clearly in j2, j4, and s4, s5, s6 (j3 represents a marginal detection). The mean observed value of I_{3429}/I_{3133} is 0.11, which again is somewhat higher than the predicted value, although the difference may be caused by deblending problems. We might be concerned that λ3432, an O3 process line, is adding to the observed λ3429 intensity. The expected value of I_{3432}/I_{3133} is given by

$$\left(\frac{I_{3432}}{I_{3123}}\right)_{\rm exp} = \left(\frac{I_{3432}}{I_{3123}}\right)_{\rm calc}\left(\frac{I_{3123}}{I_{3133}}\right)_{\rm obs}, \qquad (1)$$

where calc and obs indicate calculated (Deguchi 1985) and observed values. We infer I_{3429} by taking the product of the calculated value of I_{3429}/I_{3133} (SS) and I_{3133} from our observations. The inferred 3429 Å line intensity is then subtracted from the observed intensity of the 3429 Å feature. The residual strength should represent the observed value of I_{3432}. Using this value of I_{3432} and the observed value of I_{3133}, we determine I_{3432}/I_{3133}. Then, we compare this ratio with the value which equation (1) provides, in order to determine whether the 3432 Å line is, in fact, part of the 3429 Å blend. The value of I_{3432}/I_{3133} from our data is lower than equation (1) would predict by a factor of $\sim$2–20, in every case except the s6 spectrum. Therefore, the 3432 Å line is probably not present in these cases. For the s6 observation, the data indicate $I_{3432}/I_{3133} = 0.027$, while equation (1) gives 0.037. We regard the rough agreement as possible evidence for the 3432 Å line.

We turn now to a fuller discussion of the O3 cascades, which are all relatively weak in comparison to the O1 lines. The strongest detected O3 cascade is O III λ3123, which is the analog of λ3133 for this channel. This line is always blended with the blue wing of λ3133, making the observed line flux relatively uncertain ($\lesssim$40%). We also detect λ3407 in data

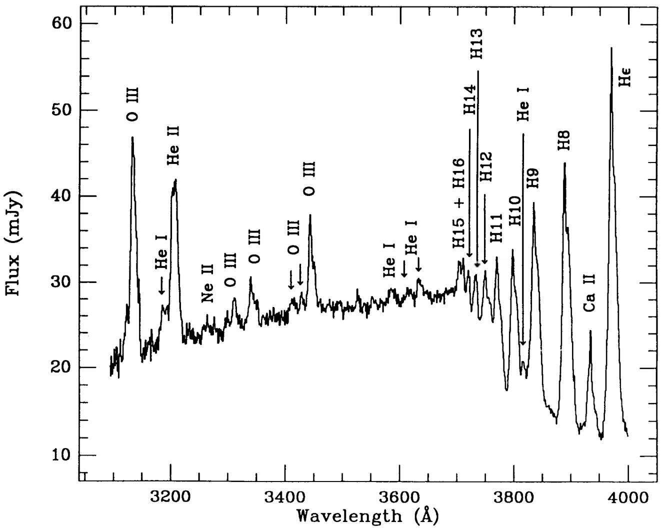

FIG. 3*a*

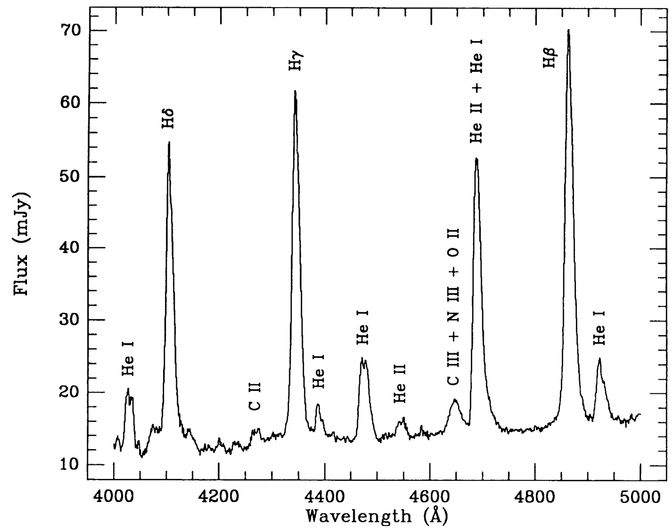

FIG. 3*b*

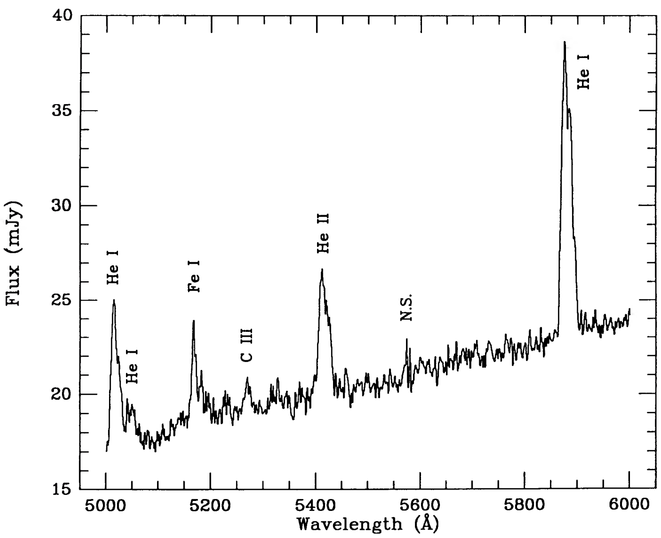

FIG. 3*c*

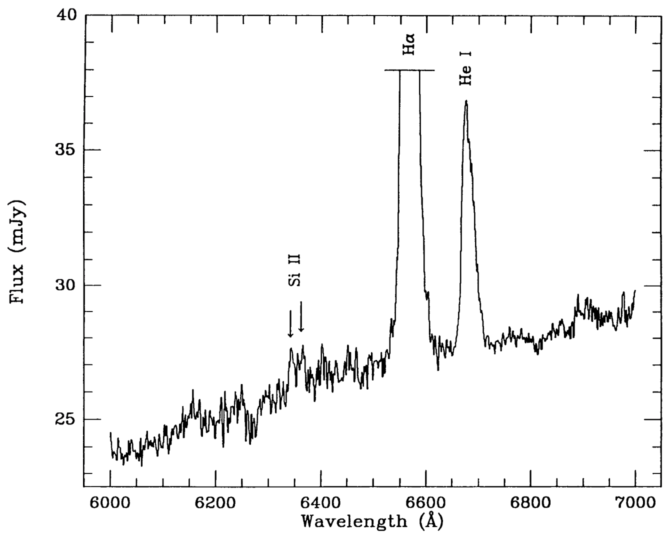

FIG. 3*d*

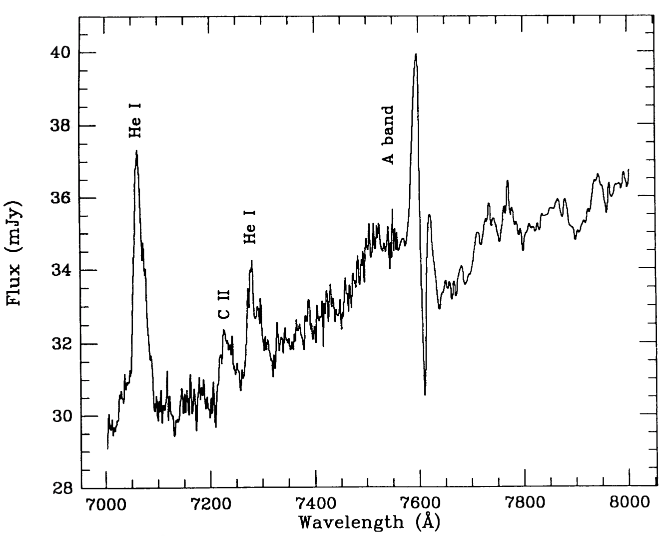

FIG. 3*e*

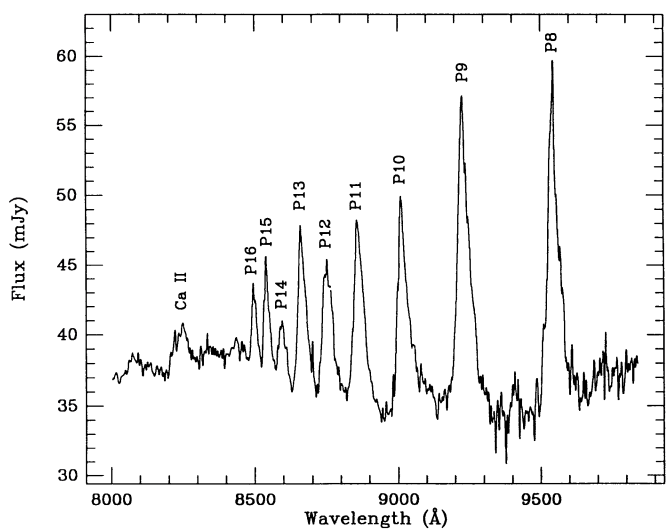

FIG. 3*f*

FIG. 3.—Spectra of AM Her from near-UV to near-IR for 1988 July 17 data, in ~1000 Å sections, except (*f*), ~1800 Å. (*a*) 3100–4000 Å region. Contains O III Bowen lines at 3123, 3133, 3299, 3312, 3341, 3407, 3429, 3444 Å. Balmer series through H16 is evident. (*b*) 4000–5000 Å region. Shows weak 4640 Å Bowen blend (see text), strong He II λ4686. Strong Balmer lines and He I lines are present. (*c*) 5000–6000 Å region. Dominated by He I and He II emission. Fe I present. (*d*) 6000–7000 Å region. Strong Hα emission, weaker He I λ6678. (*e*) 7000–8000 Å region. He I λ7065 is present. Feature near 7600 Å is poorly removed A-band absorption. (*f*) 8000–9800 Å region. Shows Paschen lines up to P8.

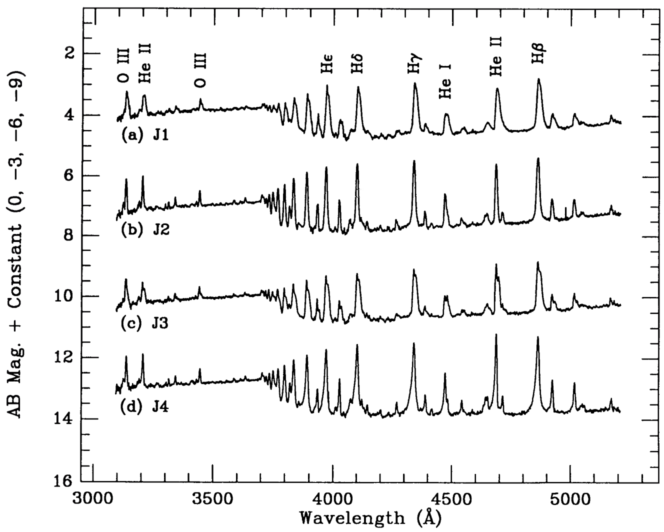

FIG. 4.—Spectra over the approximate range 3100–5200 Å from four different exposures of AM Her (notation as in Table 1): (*a*) j1. Many line profiles have peaks blueward of line center. (*b*) j2. Line profiles narrower than in (*a*), no blue peaks. (*c*) j3. Prominent blueward peaks on most lines, with He I λ4471 a notable exception. (*d*) j4. Lines narrower than in (*c*), spectrum more similar to (*b*). Strong emission lines are indicated. AB magnitude = $-2.5 \log f_\nu - 48.6$, where the units of f_ν are ergs s^{-1} cm^{-2} Hz^{-1} (Oke & Gunn 1983).

from j4, and s4, s5, s6. The range of observed values of I_{3407}/I_{3123} is 0.4–0.7, whereas atomic physics calculations predict 0.12. These values are clearly discrepant. Including a possible contribution of the O3 cascade at 3416 Å still leaves considerable discrepancy, since atomic physical calculations predict that $(I_{3407} + I_{3416})/I_{3123} = 0.22$. Thus, the feature at 3407 A probably has a substantial contribution from emission lines other than Bowen cascades. We might expect contamination by O IV λλ3404, 3401, 3412, 3414, which is seen in high-

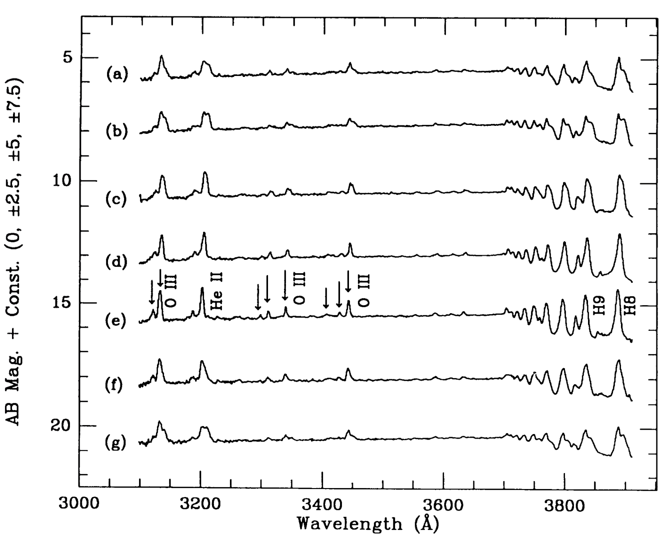

FIG. 5.—Spectra over one complete orbit of AM Her, obtained 1988 September 14 at the indicated times (UT). AB magnitude = $-2.5 \log f_\nu - 48.6$, where the units of f_ν are ergs s^{-1} cm^{-2} Hz^{-1}. (*a*) 4 : 13 (s1). (*b*) 4 : 43 (s2). (*c*) 5 : 12 (s3). (*d*) 5 : 49 (s4). (*e*) 6 : 17 (s5). (*f*) 6 : 49 (s6). (*g*) 7 : 19 (s7). In (*e*), eight Bowen lines are clearly detected (*arrows*): λλ3123, 3133, 3299, 3312, 3341, 3407, 3429, 3444. Bowen lines at 3133, 3444 Å as well as He II λ3204 are present at all phases. Note the changing structure in the Balmer lines with phase, sometimes echoed in the Bowen lines.

excitation planetary nebulae (Aller, Bowen, & Wilson 1963). Besides these lines, no additional evidence of O IV is found in our spectra of AM Her. No O IV lines were reported in *IUE* observations of this object, although we suggest that an apparent red wing on C II λ1335 (Heise & Verbunt 1988, Fig. 3) may possibly have a contribution from O IV λλ1339, 1342, 1344.

Three secondary cascades are seen in our data: λλ3299, 3312, 3341. All of these lines come from the $3p\,^3S$ sublevel, which is in turn populated by either λ3133 (O1) or λ3123 (O3). We first consider λ3341, which is the strongest observed secondary Bowen line. In the absence of the O3 process, atomic physics calculations show that $I_{3341}/I_{3133} = 0.14$ (SS). At the other extreme, if *only* the O3 process is important, then again $I_{3341}/I_{3123} = 0.14$ (Deguchi 1985). We clearly detect both O1 and O3 transitions in our data, so that some combination of the predicted values is required to compare with the observations. It is straightforward to show that

$$\left(\frac{I_{3341}}{I_{3133}}\right) = 0.14\left(1 + \frac{I_{3123}}{I_{3133}}\right), \quad (2)$$

where intensities on the right-hand side come from observations, and I_{3341} reflects the contribution from both O1 and O3. Taking the 1988 September 14 data as representative, we find that the calculated line ratios (0.16–0.18) are systematically smaller than observed values (0.20–0.27). For λ3312, we find

$$\left(\frac{I_{3312}}{I_{3133}}\right) = 0.082\left(1 + \frac{I_{3123}}{I_{3133}}\right), \quad (3)$$

with definitions as above. Observed values are in the range 0.09–0.15, whereas calculated values are 0.09–0.11. Third and weakest of the observed secondary cascades is λ3299, a line too weak for us to perform a similar analysis.

Although the differences between predicted and observed quantities are some cause for concern, the approximate agreement is encouraging. The rich variety of oxygen Bowen cascades observed in this object has never, to our knowledge, been seen in any other compact X-ray source. In particular, AM Her appears to be the first such system ever detected to have *any* cascades resulting from the O3 process. Most radiative transfer calculations of the Bowen process (e.g., Kallman & McCray 1980, hereafter KM80) have ignored O3 emission. In § 5.1, we discuss existing O3 calculations and their importance in understanding the transfer of He II Lyα.

A weak, broad emission feature centered near ~3267 Å is seen in several spectra (j4, s2, s4–s6). Comparison with line lists of planetary nebulae suggests contributions from either O III λ3261, 3265, 3267 or Ne II λλ3263, 3270. The O III lines are *not* Bowen cascades. The corresponding electronic transition, $2p3d\,^3F^o \rightarrow 2p3p\,^3D$, cannot be excited from the $^3P_2\,2p^2$ ground state by an ordinary electric dipole process, since $\Delta l = 2$. On the other hand, the lower level of the transition can produce secondary Bowen cascades. Analogously, radiative transitions from the O III $2p3d\,^3D^o$ level can populate the $2p3p\,^3P$, ^3D levels, resulting in secondary cascades. We do not expect these processes to be important, since the ^3P, ^3F levels cannot be easily excited. Collisonal excitation from the $2p3d$ level is energetically unfavorable ($\Delta E \approx 40$ eV), while the time scale for collisional excitation from the $2p3d\,^3P_2$ level is far longer (~10^6 s; Kastner, Behring, & Bhatia 1983) than the radiative lifetime of the $^3P_2$ level, ~10^{-8} s. Thus, the broad 3624 Å feature most likely is Ne II λλ3263, 3270.

Besides the O III cascades, we also detect N III Bowen lines:

$\lambda\lambda$4634, 4641, 4642. A broad emission bump centered near 4640 Å is seen in the j1–j4 data (Fig. 4). This feature may contain the N III cascades, as well as contributions from C III and O II emission lines (Paper I). In Figures 4*a* and 4*d*, the bump is blended with λ4686. Substructure in the bump is seen in Figures 4*b* and 4*c*, although the individual components cannot be separated. The nitrogen Bowen yield for the case of no O3 emission is given by $y_{\rm ON} = 8.6 I_{4640}/I_{3133}$, as shown in a parallel discussion in § V*b* of Paper I. Calculated values of $y_{\rm ON}$ from our data are typically larger than unity ($\sim$1.5), which is unphysical since the yield is a probability. Similar anomalously large $y_{\rm ON}$ values were found in our data on Sco X-1. For that case, we suggested that O3 cascades could be contributing to the overall N III emission. The expression for $y_{\rm ON}$ in this more general situation becomes

$$y_{\rm ON} = \frac{I_{4640}}{I_{3133} f_{\rm O1}/8.6 + I_{3123}(1 - f_{\rm O1})/6.0}\,, \quad (4)$$

where $f_{\rm O1}$ represents the fraction of N III cascades that come from the O1 process. Inserting typical values into the right-hand side, we find $y_{\rm ON} \approx 1.6$–1.7, so that adding the O3 lines appears to have made the problem worse. The likely resolution of this problem is that the 4640 Å bump has a significant contribution from other species. Then, by demanding that $y_{\rm ON} \leq 1$, we can get a constraint on the fractional contribution of N III lines to this bump. We find that the contribution is $\lesssim$70%.

3.1.2. He II

The He II spectrum of AM Her is relevant to the Bowen process, since He II to O III line intensity ratios are used to derive Bowen fluorescent yields. Analysis of He II line ratios in the optical spectrum is required to determine the production mechanism (e.g., case B recombination), and hence to predict the strength of He II Lyα. As in Paper II, we use the Hummer & Storey (1987) calculations for case B modified by small effects of collisions at high densities ($n_e \gtrsim 10^6$ cm^{-3}).

We detect four lines of He II: $\lambda\lambda$3204, 4542, 4686, 5411. As with the O III Bowen lines, some of these are broad enough to be blended with adjacent lines. For example, the λ3204 line (He II Paschen-β or Pβ) pictured in Figure 3*a* has a weak He I λ3188 line blended with its blue wing. We have already mentioned that the blue wing of λ4686 (Pα; Fig. 3*b*) is blended with the N III Bowen lines. Also, it is evident that sometimes a line is blended with the red wing of λ4686 (He I λ4712; also see Fig. 4). The Brackett series line λ4542 (Br9; Fig. 3*b*), detected in all the spectra in Figure 4, is often relatively faint. The λ5411 line (Brγ; Fig. 3*c*) is detected only in the j1 spectrum, since all other observations covered the spectral region $\lesssim$5200 Å.

There is some suggestion of multiple components in the stronger He II lines, namely $\lambda\lambda$3204, 4686. We find that the flat-topped profile of λ3204 from j1 (Fig. 4*a*) can be fit, albeit poorly, by a sum of two Gaussians of equal width. The blueward and redward components, separated by $\sim$650 km s^{-1}, have different intensities, with $I_{B\,3204}/I_{R\,3204} \approx 1.2$, where the notation *B* and *R* indicates blue and red components. The corresponding λ4686 profile in this spectrum unfortunately does not admit to a similar analysis. However, the apparent shape of λ4686 in Figure 4*a* is at least qualitatively consistent with two components, the stronger one being blueward.

In the j3 spectrum (Fig. 4*c*), we see a marked similarity in the λ3204 and λ4686 profiles. A Gaussian deblending analysis of λ3204 is only approximate, again because of the poor fits. In particular, there are problems fitting the narrow peak of the blue component, as well as the broad long-wavelength wing of the red component. The velocity separation of the line centroids is similar to that derived above. However, this velocity difference should *not* be interpreted as a general property of AM Her around the orbit. We emphasize that the j1 and j3 spectra (Figs. 4*a* and 4*c*) were obtained at similar phases (0.58 and 0.71; Table 1). In fact, there is no evidence for a multiple component structure in $\lambda\lambda$3204, 4686 in spectra taken at two other orbital phases (0.36 and 0.00; Figs. 4*b* and 4*d*). For the j3 data, the ratio of intensities is also not very different from before ($I_{B\,3204}/I_{R\,3204} \approx 1.1$). A good fit is achieved for λ4686 in this data set. The line is resolved into two components, separated by 640 km s^{-1}. The red component is broader (FWHM $\approx$ 730 km s^{-1}) than the blue one (FWHM $\approx$ 350 km s^{-1}), and we find ($I_{B\,4686}/I_{R\,4686} \approx 0.85$). The widths derived from the Gaussian fit have been corrected for the instrumental resolution of $\sim$4.5 Å. The expected shift of the line centroid during typical integration times of 200 s is only $\sim$80 km s^{-1}. Since this term adds in quadrature, we conclude that smearing of the line profile because of velocity changes at the source has a minimal effect on the derived FWHM values (<3%). In earlier work, Greenstein et al. (1977) found that λ4686 consisted of a broad (FWHM $\approx$ 700 km s^{-1}) and a narrow (FWHM $\approx$ 90 km s^{-1}) component.

Ideally, to test whether case B recombination applies to the He II emission line spectrum in AM Her, we would prefer to have many independent diagnostics. However, given that we have detected only four emission lines of He II, we have only a limited number of observed line ratios. Another complication is that the separate components observed in individual lines (e.g., λ4686) could conceivably arise in physically distinct regions. In this case, the blue component of a line might satisfy case B, while the red component might not. Our inability to separate the blue component from the red one complicates this issue. Nevertheless, if physical conditions depart from case B, we expect (from the high densities inferred in § 4) that the intrinsic line decrements will always be *flatter* than case B. This argument provides a resolution to the problem of different mechanisms producing the red and blue components. Clearly, if the line ratio of one of these two components is case B, while the other is flatter than case B, the ratio of summed (red + blue) intensities will also be flatter than case B. In this case, observed line decrements derived from summed intensities, [e.g., $(I_{R\,3204} + I_{B\,3204})/(I_{R\,4686} + I_{B\,4686})$], provide a lower limit to the deviation from case B.

We use the technique of taking ratios of summed intensities for measuring all He II line ratios. The inferred He II Paschen decrement (Pβ/Pα) is flatter than case B. We find $0.61 \leq I_{3204}/I_{4686} \leq 0.87$, while the case B result is 0.46–0.49 for the derived He II zone temperature of 20,000–38,000 K (§ 5.2). Because the case B line ratios for He II vary by only $\sim$3%–5% over the temperature range of interest, we simply adopt temperature-averaged values. A flat decrement is also found for the Brackett lines, Br9/Brγ, where the observed value is $I_{4542}/I_{5411} = 0.53$, compared to 0.46 from case B. The deviation from theory is larger for Br9/Pα (observed ratio: 0.16, calculated ratio: 0.083) and Brγ/Pα (observed ratio: 0.084, calculated ratio: 0.038). Our observations of Br9/Pα, Br9/Brγ, and Brγ/Pα show largely the same trend as those of S77.

Because the strong λ3204 and λ4686 lines in AM Her are somewhat blended with adjacent lines, we emphasize again that the line ratio I_{3204}/I_{4686} is only approximate. An independent measure of the observed value of I_{3204}/I_{4686} is provided by another approach: when the line profiles of $\lambda 3204$ and $\lambda 4686$ in a given spectrum are superposed (with velocity on the abscissa), we can simply scale up the value of each point in the $\lambda 3204$ profile by a factor $f_{\rm sca}$ to match the $\lambda 4686$ shape (by eye). This technique works equally well when the He II lines have single or double components (Fig. 6). The line intensity ratio is then given by $I_{3204}/I_{4686} = f_{\rm sca}(4686/3204)$. We find in each of the four spectra in Figure 4 that the line ratio is smaller than derived above, by 15%–25%. This result is expected, since the major contaminant is the contribution to $\lambda 3204$ from He I $\lambda 3188$. The range of values, $0.53 \leq I_{3204}/I_{4686} \leq 0.73$, is smaller, but still largely exceeds the case B result. We discuss possible line formation mechanisms, including effects of large optical depths in the He II emission lines, in § 4.

3.1.3. H I

Clearly, the strongest H I feature is the Balmer discontinuity, which is prominent in Figure 2. The line spectrum of the Balmer series is detected up to H16, which is blended with H15 (Fig. 3*a*). We see in this figure that the H12 line is distinct from other Balmer lines in that it is partly blended with another line on its red wing. The blended feature has approximately the correct wavelength and intensity to be yet another Bowen emission line, O III $\lambda 3760$, but it might also be He I $\lambda 3756$. H10 and H9 form a blend with He I $\lambda 3820$ in Figure 3*a*. Low-order series members (Fig. 3*b*) include Hδ, Hγ (very slightly blended with He I $\lambda 4388$ on the red wing), and Hβ. These lines appear to have different structure than the neighboring lines of He I.

Apparently, our work is the first to show the Paschen lines and Paschen discontinuity in AM Her. The discontinuity is clearly seen in Figure 2. Strong Paschen emission lines, P8–P16, are observed. High-order lines are pictured in Figure 3*f*. Although P15 and P16 have blended wings, the other lines down to P11 are relatively clean. The P14 line is anomalously weak. Turning to Figure 3*a*, we see that the lines P10, P9, and P8 all have noisy red wings. The continuum near P8 is somewhat uncertain, since the line falls near the edge of a scan.

The H I emission lines appear to possess red and blue com-

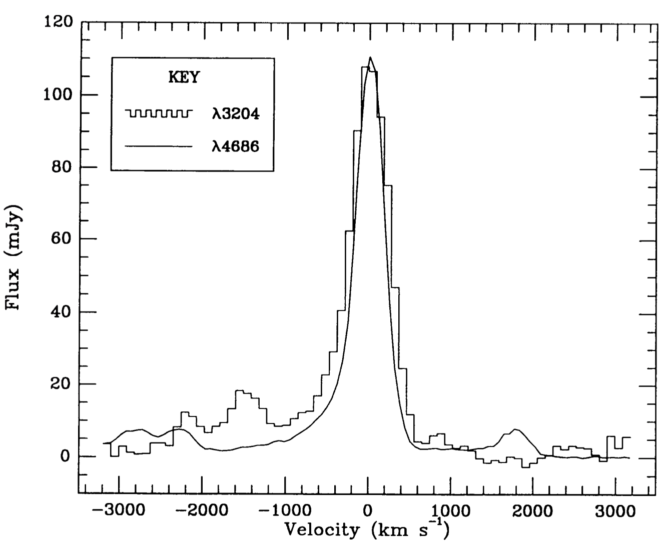

FIG. 6.—Superposition in velocity space of He II $\lambda 4686$ and He II $\lambda 3204$ profiles of AM Her, with I_{3204} scaled up by a factor of 2.7. Data are from j4 observations. We infer $I_{3204}/I_{4686} \approx 0.54$ from this analysis.

ponents, similar to the He II lines already discussed. For the Balmer lines, our data indicate that the relative strengths of the two components vary with binary phase, as shown in Figure 5. We see that H8–H12 all exhibit a strong, narrow blue component, with the suggestion of a weaker red component, near $\phi = 0$. The separation between red and blue components diminishes going toward $\phi = 0.25$, until we find a single-peaked profile near $\phi = 0.5$. There is some suggestion that the same behavior is present in the stronger non-Balmer lines, including O III $\lambda\lambda 3133$, 3444 and He II $\lambda 3204$ (Fig. 5*a*). Based on a fit we performed to the blue centroids of H8–H10, the overall velocity structure as a function of binary phase is similar to that found by Greenstein et al. (1977) for the sharp (FWHM ≈ 90 km s^{-1}) component of He I $\lambda 4471$. It is instructive to compare our observations with those of Crampton & Cowley (1977), who studied the phase dependence of the profiles of Hϵ and Hδ in this system. In marked contrast to our data, these authors found that both lines have a strong, narrow *red* component, which is most obvious at $\phi = 0$ (see their Fig. 2). Despite this important difference, they also found that the profile becomes gradually more single-peaked as ϕ approaches 0.5.

We now use the total line intensity ratios to quantify the hydrogen line decrements in our observations. The Balmer decrement is significantly flatter than that expected from case B recombination, for temperatures in the range 10,000–30,000 K (§ 4.2). We adopt temperature-averaged values from case B calculations, since the calculated line ratios are constant with temperature to $\sim 5\%$. For the j1 data we find Hα:Hβ:Hγ:Hδ = 0.82:1.00:1.07:1.01, compared to 2.72:1.00:0.48:0.27 for case B. The other data show the same trend. We find Hβ:Hγ:Hδ = 1.00:1.01:0.97, 1.00:0.94:0.92, and 1.00:1.04:1.18 for j2–j4. Thus, we obtain a mean value of Hα:Hβ:Hγ:Hδ = 0.82:1.00:1.02:1.01. The Paschen lines are also stronger relative to Hβ than expected from case B, by approximately a factor of 10. Interestingly, the observed Paschen decrement is *steeper* than case B. We find from our data P9:P10:P11:P12 = 1.0:0.60:0.46:0.32, which can be compared to the case B value of 1.0:0.74:0.56:0.44. However, the observational determination of these high-order Paschen line fluxes is uncertain. The Stark-broadened line profiles mask the true underlying continuum (Fig. 3*f*), so that we systematically underestimate line fluxes. This phenomenon may also affect the high-order Balmer lines ($\geq$H8), and other lines shortward of H8 and longward of the Balmer discontinuity. To reflect this, we have explicitly noted the affected intensities as lower-limit values in Tables 2 and 3. In § 4, we use the observed Balmer decrement to constrain the physical conditions in the H I zone.

3.1.4. He I *and Other Emission Lines*

Besides the strong H I lines, the next most common species in our spectra is He I. The triplet lines are represented by $\lambda\lambda 3188$, 3587, 3634, 3820, 4026, 4471, 4713, 5876, 7065. We also see the following singlet lines: $\lambda\lambda 3614$, 3756, 4144, 4388, 4922, 5016, 5048, 6678, 7281. Additional lines may be blended with other lines in the spectrum. The observed line ratios are in poor agreement with case A recombination calculations (Brocklehurst 1972), although for the metastable $2s\,^3S$ level collisional excitation and optical depth effects may be important (e.g., Osterbrock 1989, Chap. 4). We give some representative values for j1. The observed decrement for the $nd\,^3D \rightarrow 2p\,^3P$ lines is relatively flat: $I(n=3):I(n=4):I(n=5) =$

$I_{5876}:I_{4471}:I_{4026} = 0.78:1.00:0.66$, compared to recombination values of 2.56:1.00:0.49 at 2×10^4 K. In the singlet spectrum, the high optical depths inferred in the He II and H I lines suggest that case B recombination will be a reasonable approximation. We find a flat decrement for the singlet transitions. For the $nd\,^1D \rightarrow 2p\,^1P$ lines, $I(n = 3):I(n = 4):I(n = 5) = I_{6678}:I_{4922}:I_{4388} = 0.87:1.00:0.61$, as opposed to the calculated value of 2.68:1.00:0.48. For I_{4388}, which is blended in the j1 observation, we have used the average of the j2–j4 observations.

Although hydrogen and helium account for the great majority of the observed emission lines, we also detect a few strong lines of other species. Notable of these is Ca II λ3933, which provides some insight into H I zone densities. The detection of λ3933 implies the presence of Ca II λ3968, since both lines are radiative transitions from the $4p\,^2P$ level. Presumably, Ca II λ3968 in our spectrum is blended with Hϵ. We estimate the strength of the 3968 Å line, assuming that the low-lying (∼3.2 eV) $4p$ state is collisionally excited from the $4s$ ground state, and using published Ca II collision strengths (Taylor & Dunn 1973; Osterbrock & Wallace 1977). The result is $I_{3968}/I_{3933} = \frac{1}{2}$, so that λ3968 makes a contribution of only 6%–10% of the total Hϵ intensity. In addition, the absence of collisional de-excitation of Ca II λ3933 provides a density constraint: $n_e < 7.1 \times 10^{14}$ cm^{-3}. This limit is relatively insensitive to temperature. Ca II λλ8202, 8249, 8255 is also detected in our data.

Other emission lines in our data are Fe I λ5172; possibly C II λ4267; C II λλ7231, 7236, 7237; Si II λλ6347, 6371; and a blend at 4071 Å that probably contains C III λλ4069, 4070, 4072 and O II λλ4070, 4071, 4072 (see Fig. 3b). A weak emission feature detected near 5271 Å (Fig. 3c) is probably C III λ5273. The electronic transition ($2p3p \rightarrow 2p3s$) is similar to that which produces the observed set of C III lines at 4647–4650 Å ($2s3p \rightarrow 2s3s$), features that form a part of the 4640 Å bump.

3.2. *EF Eridani*

The co-added spectrum of EF Eri is displayed in Figure 7, and Table 4 provides a list of line fluxes. As in AM Her, the spectrum of EF Eri shows a strong Balmer discontinuity. The Balmer decrement appears to be relatively flat, with prominent high-order series members. Bowen lines (Fig. 1) are again evident, and dominate the emission shortward of the Balmer discontinuity. EF Eri shows strong O III λλ3133, 3341, 3444. A small blue component of λ3133 may represent a contribution from λ3123, an O3 cascade. However, the strength of λ3123 would be small in comparison to λ3133 (≲10%). Other than this line, we found no additional evidence for the O3 process in EF Eri. The O III λ3312 Bowen line is marginally detected, although the observed value of I_{3312}/I_{3133} agrees poorly with atomic physics calculations. For I_{3341}/I_{3133}, we find better agreement. The observed value is 0.17, whereas the calculated value (SS) is 0.14. Also, the value we measure for I_{3444}/I_{3133} agrees well with theory. Besides the O III emission, we detect the 4640 Å bump, which probably has a contribution from the nitrogen Bowen lines. The observed nitrogen Bowen yield for the case of no O3 pumping (§ 3.1), $y_{\rm ON}$, is again larger than unity (2.92). Because no O3 line is directly observed, we cannot estimate the effect of these lines on production of N III cascades. However, by again demanding $y_{\rm ON} \leq 1$, we find an upper limit of 33% for the contribution of nitrogen Bowen lines to the overall 4640 Å bump.

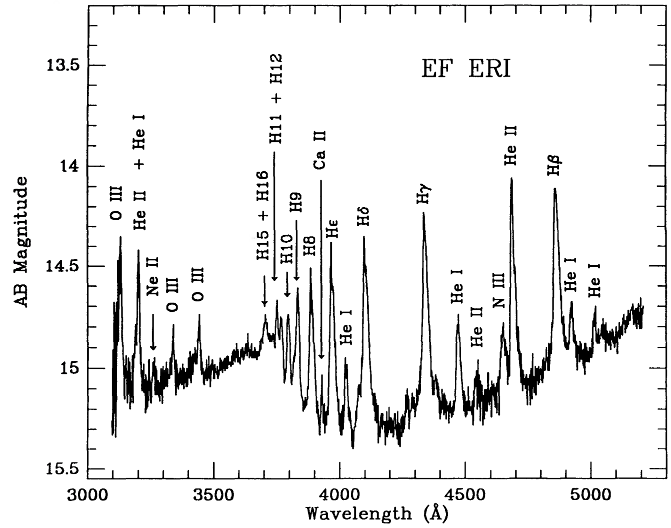

FIG. 7.—Complete spectrum of EF Eri over the range 3100–5200 Å. Bowen lines at 3133, 3312, 3341, 3444 Å are evident. Balmer lines are present through H16. The N III 4640 Å bump appears in the blue wing of He II λ4686.

The He II Paschen lines Pα and Pβ are again detected. Both are blended with lines on the blue wings, λ3204 with λ3188, and λ4686 with the 4640 Å bump. For λ4686, the blending is more severe. The observed I_{3204}/I_{4686} ratio is 0.57, which is appreciably larger than the case B recombination value. Of the detected H I Balmer lines, H15 is blended with H16, while H13 and H14 appear to be oddly absent. The lines H12 and H11 are blended, as are H10 and H9. Three of the

TABLE 4

EF ERI LINE INTENSITIES[a]

Ion	λ	$f_\nu(\lambda)$
O III	3133b[b]	0.150
He I	3188	0.033:
H II	3204	0.088
Ne II	3267[c]	0.009
O III	3312	0.004:
O III	3341	0.026
O III	3444	0.044
H15 + H16	3704	>0.021
H14	3722	...
H13	3734	...
H12 + H11	3761	>0.046
H10 + H9	3817	>0.113:
H8	3889	0.099
Ca II	3933	0.011
Hϵ	3970	0.129
He I	4026	0.037
Hδ	4102	0.194
Hγ	4341	0.240
He I	4471	0.056
N III	4640b[d]	0.051:
He II	4686	0.155:
Hβ	4861	0.188
He I	4922	0.029
He I	5016	0.013

[a] Wavelengths in Å, intensities in units of 10^{-12} ergs cm^{-2} s^{-1}. Line blends indicated by a b. Lower limits are for lines where Stark-broadened wings of lines caused an underestimate of flux.

[b] May contain a contribution from O III λ3123.

[c] Blend of Ne II λλ3263, 3270.

[d] May contain contributions from O II and C III; see text.

strongest Balmer lines, Hδ, Hγ, and Hβ, appear to possess both broad and narrow components. However, it is difficult to separate the components at our spectral resolution of $\sim$4.5 Å. Plotting these lines in velocity space (as we did in Fig. 6), we find that the profiles are virtually identical, except for a constant scaling factor. The red wing of Hβ appears to be blended with He I λ4922. We infer a Balmer decrement of Hβ:Hγ:Hδ = 1.00:1.28:1.03, compared with the significantly steeper case B value of 1.00:0.48:0.26. The observed Balmer decrement is somewhat similar to that of AM Her (1.00:1.02:1.01). Also, we again find that strong Stark broadening affects determination of the high-order Balmer line fluxes ($\geq$H8), and other lines longward of the Balmer discontinuity and shortward of H8. We quote lower-limit values for the affected lines (Table 4), as for AM Her.

Five lines of neutral helium are seen in the spectrum of EF Eri: He I $\lambda\lambda$3188, 4026, 4471, 4922, 5016. As for AM Her, the line ratios differ significantly from recombination calculations. For example, we find $I_{4471}/I_{4026} = 0.68$, compared to the calculated value of 0.48. In addition to the hydrogen, helium, and Bowen lines, we also detect Ca II λ3933. We again assume that the calcium line emission is produced by collisional excitation of the ground state. This approach shows that blended Ca II λ3968 is expected to account for only $\sim$4% of the total measured Hϵ intensity. The absence of collisional deexcitation of Ca II λ3933 implies that $n_e < 7.1 \times 10^{14}$ cm^{-3} in the H I zone.

4. ANALYSIS OF H I AND He II

4.1. *Observed Continuum of AM Herculis*

At first glance, the observed continuum of AM Her (Fig. 2) is similar to what would be expected for continuous emission from a pure thermal hydrogen plasma (e.g., Osterbrock 1989, Fig. 4.1). The monochromatic volume emissivity takes the form $j(\mathrm{H\ II})_\nu = n_{\mathrm{H\ II}}\, n_e\, \gamma_\nu/(4\pi)$, where γ_ν has a contribution from both free-free (bremsstrahlung) and free-bound (radiative recombination) processes. Two-photon continuum emission is not expected to be significant, given the electron densities ($>10^{11}$ cm^{-3}) we derive in § 5. If the temperature lies close to the lower limit value of $\sim$7000 K found in § 4.2, then the principal free-bound processes are H I Balmer emission for $\lambda < 3647$, and Paschen emission for $3647 < \lambda < 8204$. However, since we cannot rule out significantly higher temperatures, some recombinations to the $n = 3$ and higher levels may produce a significant amount of $\lambda < 3647$ emission. The ratio of free-free to free-bound emission also increases with temperature. We refer to the sum of bremsstrahlung and recombination emission simply as Balmer- or Paschen-continuum emission.

For pure recombination continua of hydrogenic species, the emissivity is proportional to $(kT)^{-3/2} \exp{(-h\,\Delta\nu/kT)}$, where $h\,\Delta\nu$ is the photon energy measured from threshold. The steepness of the observed Balmer continuum thus provides a temperature diagnostic. This technique was invoked by Williams et al. (1978) for the temperature determination of the nova shell around DQ Her. We have attempted to use the technique to estimate the temperature in the Balmer emission region of AM Her.

All calculations were done for the j1 spectrum, pictured in Figure 2. First, we tried to model the observed continuum by pure hydrogen continuum emission—a sum of thermal bremsstrahlung and recombination to all levels up to $n = 3$—at a fixed value of T. Results are presented in Figure 8*a*. At lower temperatures ($\sim$10,000–20,000 K), the model satisfactorily fits the observed recombination continuum slopes, but considerably overestimates the size of the discontinuities. On the other hand, in hotter models ($T \approx 30{,}000$ K) the sizes of the Balmer and Paschen jumps are well approximated, whereas the slope of both the Balmer and Paschen continua are not. In a second attempt, we used a two-temperature model, in which the theoretical continua are simply summed. This approach also fails, since the co-added continuum merely mimics the predicted shape at a T value intermediate between the two temperatures.

It seems likely that the poorness of the fits is caused by contributions to the continua from other sources in the AM

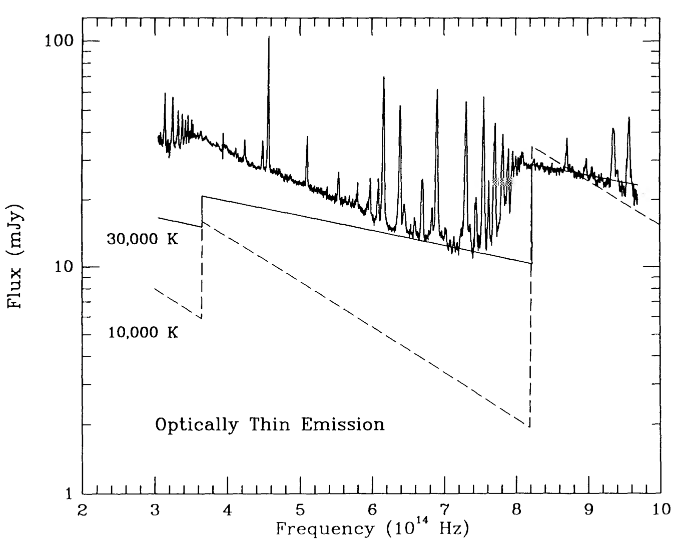

FIG. 8*a*

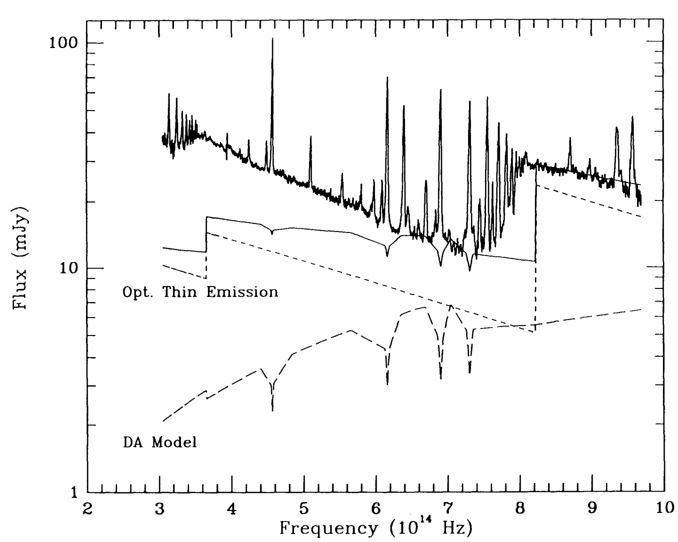

FIG. 8*b*

FIG. 8.—Fits to observed continuum of AM Her (j1 observation). (*a*) Single temperature hydrogen continuum emission (bremsstrahlung + recombination) fits. A comparison of 10,000 K (*dashed line*) and 30,000 K (*solid line*) optically thin emission to the observed continuum. (*b*) Like (*a*), but expected emission from white dwarf photosphere (*large dashes*) is added to optically thin emission (*small dashes*). The sum of these two is shown as a solid line. The Balmer continuum is well matched, but Balmer absorption lines are problematic.

Her binary system. Since the secondary star is known to be very red (~M4.5 V; Young & Schneider 1979), it cannot contribute significantly to the near-UV/optical continuum. On the other hand, the white dwarf may have some effect. Heise & Verbunt (1988) showed that the *IUE* spectrum of AM Her is well approximated by published models of DA white dwarf photospheres. Because of the exponential dependence of Balmer continuum emission, the short-wavelength region of the *IUE* data ($\lambda \lesssim 1800$) should be dominated by *non*-Balmer continua. Heise & Verbunt found $T_{\rm eff} = 20{,}000$ K at a white dwarf radius $R_{\rm WD} = 1.1 \times 10^9$ cm and a distance to the source $D = 75$ pc. We attempted to fit the observations of AM Her with a sum of the model white dwarf spectrum and a pure hydrogen plasma (see Fig. 8*b*). Acceptable fits are obtained for the size of the Balmer discontinuity and the slope of the Balmer continuum. In our model, the predicted Paschen continuum is unacceptably flatter than in the observed spectrum. This model also predicts strong Balmer absorption lines, arising in the white dwarf photosphere. Such absorption lines are not seen in our spectra of AM Her. Perhaps the absorption lines are partly filled by Balmer emission lines coming from regions near the white dwarf. If emission lines come from the heated face of the secondary, the absorption would probably not be filled in at all phases.

In expectation of the results of § 4.2, we considered the possibility of introducing a small opacity into the Balmer continuum. The contribution of the white dwarf photosphere, which is relatively unimportant to the shape of the Paschen continuum, was not included. If the continuum emission region is modeled as a geometrically thin, but optically thick slab (hereafter, thin slab), then the predicted emissivity is simply scaled by the escape probability from the slab: $[1 - \exp(-\tau_\nu)]/\tau_\nu$, where τ_ν is the monochromatic continuum optical depth. The models continue to have difficulty fitting the Paschen continuum. For $T \gtrsim 15{,}000$ K and a Balmer edge opacity given by $\tau \lesssim 1$, the results are consistent with those of § 4.2.

This concludes our analysis of the observed continuum of AM Her. A more detailed model may be required to explain the observed Paschen continuum. In the red end of the spectrum, we expect contributions from cyclotron emission and the secondary star. However, the observed continuum longward of Hβ is almost a straight line in $\log f_\nu$–ν space. It seems rather peculiar that in AM Her the cyclotron, free-free, and optically thick Paschen recombination components combine to produce such a simple spectrum.

Although our analysis focused only one point in binary phase (j1), it would be interesting to study the shape of the full near-UV to near-IR continuum of AM Her around the orbit. At different binary phases, the changing path length through the absorbing region along our line of sight may be evident as variability in the size of the Balmer discontinuity. This assumes that the geometry resembles a slab. The Balmer lines would not show similar behavior, since typical opacities (see below) are probably large, regardless of the viewing angle.

4.2. H I *Line Ratios*

In addition to using observed continua to set constraints on opacity and temperature, we can also use the line ratios of H I Balmer and Paschen lines to develop similar limits. S77 suggested that the anomalously flat Balmer decrement could be explained by assuming large optical depths in the Balmer lines. They modeled the measured flux, F_i, in any given Balmer line i by

$$F_i = B(\nu_i, T)[1 - \exp(-\tau_i)]\Delta\nu_i\,, \tag{5}$$

where $\Delta\nu_i$ is the line width. This approximation assumes that τ_i is strongly peaked around line center, implying that the line is dominated by a Doppler core. Also, $\tau_i \propto f_i \Delta\nu_i^{-1}$, where f_i is the f-value of the particular line, and the proportionality constant is the same for all Balmer lines (e.g., Rybicki & Lightman 1979). S77 assume that $\Delta\nu_i \propto \nu_i$, which is true in the Doppler core. These authors performed a least-squares fit to the observed line ratios Hα/Hϵ, Hβ/Hϵ, Hγ/Hϵ, and Hδ/Hϵ. The two free parameters were T and $\tau_{\rm H\epsilon}$, for which they found $T = 9600 \pm 1100$ K and $\tau_{\rm H\epsilon} = 0.81 \pm 0.15$, or equivalently $\tau_{\rm H\alpha} = 67 \pm 12$.

The S77 analysis can be questioned in two respects. First, the errors are significantly underestimated. As noted by Lampton, Margon, & Bowyer (1976), a confidence level of 1 σ for a two-parameter fit requires $\Delta\chi^2 = 2.3$, whereas S77 used $\Delta\chi^2 = 1$. Lampton et al. prefer a 90% confidence level for multiparameter fits, implying $\Delta\chi^2 = 4.6$. Therefore, the 90% and 99% confidence limits are taken as measures of the uncertainty for this discussion. The second and more serious objection to the S77 approach is their use of equation (5) as exact. This relation is applicable only in the limit of small line opacity, corresponding to the linear portion of the curve of growth. At line-center optical depths of ~10–100, the line core begins to saturate, and $\Delta\nu$ scales less rapidly with ν than linearly. Such large line opacities are not unexpected for AM Her, given our analysis of the observed Balmer continuum (§ 4.1). On the other hand, the damping wings are relatively unimportant, since we find $\tau \leq 10^4$ for most of the lines. Thus, rather than estimating the line flux as the product of $\Delta\nu$ and the amplitude of the line-center Doppler profile, we explicitly integrate over the line.

We fitted the data for Balmer lines Hβ–H8 (and Hα for j1) relative to Hϵ using the frequency-dependent opacities. The fits are generally good, with $\chi^2 \approx 1$ for the 2 or 3 remaining degrees of freedom. However, the 90% and 99% confidence limits suggest that a large range of parameter space is allowed by our fits (Fig. 9*a*). The fit values of $\tau_{\rm H\alpha}$ and T are strongly coupled. Generally, $T \gtrsim 7000$ K and $\tau_{\rm H\alpha} \gtrsim 100$, although no clear upper limits are indicated in our analysis. For $T \gtrsim 30{,}000$ K, all the Balmer line frequencies are on the Rayleigh-Jeans tail, so that the decrement is essentially temperature independent.

To complete the general discussion of the observed Balmer decrement in AM Her, we give brief mention to non–LTE effects as an explanation. Elitzur et al. (1983) suggested that instead of high electron densities ($\gtrsim 10^{13}$ cm^{-3}), which drive the source function toward LTE, stimulated emission might account for the observed decrement. This process requires high line opacities (corrected for stimulated effects) but can occur at densities low enough that LTE is not yet achieved (e.g., $n_e = 10^{11}$ cm^{-3}). The authors predict Hα:Hβ:Hγ:Hδ = 0.90:1.00:0.81:0.62, in the limit of high radiation field. This can be compared to the mean observed decrement (§ 3), 0.82:1.00:1.02:1.01. The agreement is relatively poor. For Hα, the discrepancy is small enough so that we cannot rule out this mechanism. The large discrepancies with Hγ and Hδ, however, probably indicate that stimulated effects are unimportant for these lines.

For EF Eri, we have noted in an earlier section that the

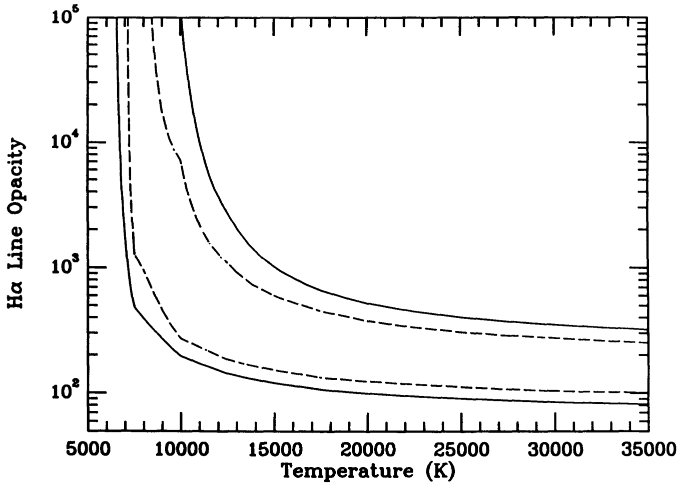

FIG. 9a

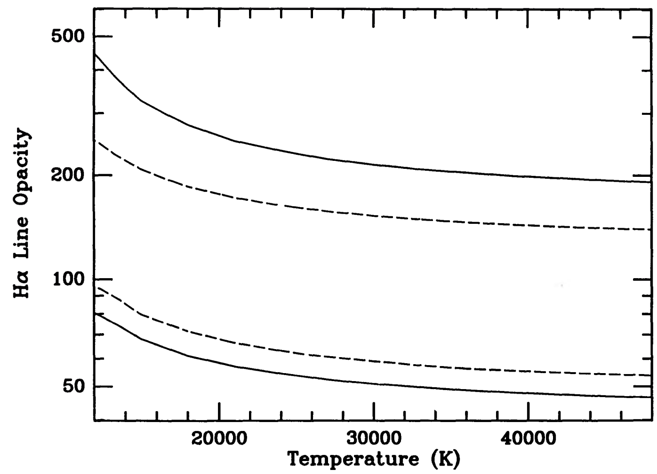

FIG. 9b

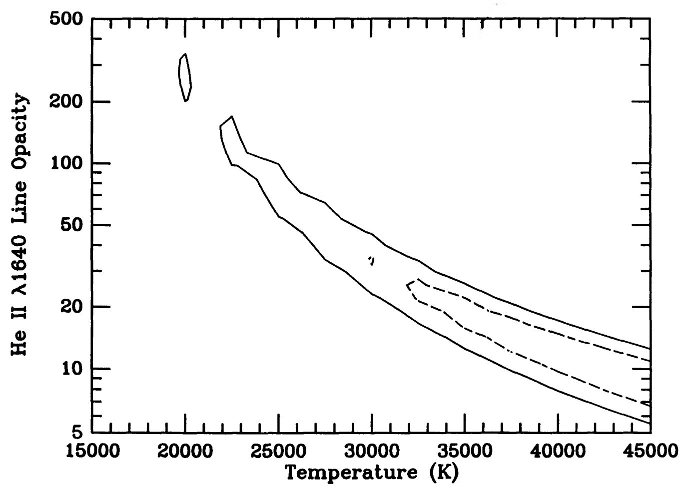

FIG. 9c

FIG. 9.—Confidence figures for fits to line ratios. In each case, the 90% contour (*dashed line*) and 99% contour (*solid line*) are shown. (*a*) Fit to H I Balmer lines for AM Her for j2 observation. (*b*) Fit to H I Balmer lines in EF Eri. (*c*) Fit to He II lines in AM Her (j1 observation).

observed Balmer decrement is significantly flatter than the case B recombination value. We attempted to apply the simple thin slab analysis to the observed ratios of Hβ, Hγ, Hδ, Hϵ, and H8, relative to Hϵ. The fits are not terribly constaining for the temperature, and we obtain a lower limit of $T \gtrsim 12{,}000$. The allowed line opacities fall in the range $\tau_{\mathrm{H}\alpha} \approx 30$–$300$ (Fig. 9*b*). Typical values of χ^2 were 1.6–3.5 for the remaining 2 degrees of freedom.

4.3. He II *Line Ratios*

For AM Her, we applied the thin-slab approach described in the previous section to model the observed intensities of He II λλ3204, 4542, 5411 relative to λ4686. Level populations are assumed to be in LTE for calculating the optical depths of lines from levels with different principal quantum number. The two free parameters are temperature and τ_{1640}, the optical depth expected for He II λ1640 (Balmer α). An acceptable fit is achieved, with $\chi^2_{\mathrm{min}} \approx 1$ for the 1 degree of freedom. As for the H I lines in AM Her, the allowed line opacities and temperatures are correlated (Fig. 1*c*). We find $T \gtrsim 20{,}000$ K and $\tau_{1640} \lesssim 200$. The implications of the high He II line opacities in interpreting the Bowen process in this object are discussed below, while tighter constraints on the temperature and opacity in the He II zone are discussed in § 5.2.

5. INTERPRETATION OF BOWEN LINES

5.1. *O3 Process*

As discussed earlier in this work (§ 3.1), we find strong evidence for the presence of the O3 process in AM Her. The most irrefutable data are the multiple detections of O III λ3123, which can only be produced by He II Lyα conversion to O3. Curiously, published radiative transfer calculations have generally ignored the relevance of O3 cascades to the Bowen process, although Harrington (1972) gives a preliminary discussion. These calculations therefore assumed that Bowen conversion occurs only in the Doppler core of He II Lyα, since the O3 line is in the (red) damping wing of Lyα under typical conditions. Deguchi (1985) needed to posit an improbable geometry in order to distort the effective He II Lyα profile seen by an O III ion; he then found that O3 could be produced, with a yield value ∼0.2 of the corresponding O1 value.

A more physical argument for the O3 process can be found in a recent paper by Neufeld (1990a). He considered the transfer of He II Lyα in the limit of high line-center opacity ($\tau_L \gtrsim 10^5$). In this limit, the damping wings of He II Lyα become important to the transfer. Neufeld performed a simplified calculation, assuming that conversion to a Bowen line is the only possibility for He II Lyα, which is valid for the range of opacities used (KM80). Also, he assumed $n_e \lesssim 10^4$ cm^{-3}, so that collisional effects can be ignored (Neufeld 1990b). Neufeld (1990a) derived the expected ratio of O3 to O1 pumping rates ($R_{\mathrm{O3}}/R_{\mathrm{O1}}$) of the $2p3d\,^3P^o$ level, as a function of the ionic ratio $n_{\mathrm{O\,III}}/n_{\mathrm{He\,II}}$ for $10^5 \lesssim \tau_L \lesssim 10^{6.5}$, and for $\tau_L \to \infty$. The quantity $R_{\mathrm{O3}}/R_{\mathrm{O1}}$ is a decreasing function of $n_{\mathrm{O\,III}}/n_{\mathrm{He\,II}}$. This is because at higher relative O III excitation, a He II Lyα photon is increasingly likely to encounter an O III ion before the photon has a chance to diffuse significantly in frequency.

Neufeld's work suggests that the strong O3 lines which we observe in AM Her and EF Eri are also produced by a considerably broadened He II Lyα profile. Collisional effects not considered in the Neufeld (1990a) calculation are relevant at our derived densities ($> 10^{11}$ cm^{-3}), so that a direct interpretation of the calculated $R_{\mathrm{O3}}/R_{\mathrm{O1}}$ values is not possible. However, we can derive R_{O3}/R_{O1} independently from observed quantities. Both $\lambda 3133$ (from O1) and $\lambda 3123$ (from O3) are detected in our data for AM Her. For EF Eri, we detect $\lambda 3133$ and have an upper limit for $\lambda 3123$. Because these two lines each result from the $2p3d\,^3P^o$ excited state, we may write

$$\frac{R_{O3}}{R_{O1}} = \frac{I_{3123}}{I_{3133}} \frac{A_{3133}}{A_{3123}} \frac{3123}{3133}, \tag{6}$$

where A_{3123} and A_{3133} are Einstein A-coefficients. Taking the atomic data from SS and Deguchi (1985), we find $R_{O3}/R_{O1} = 0.25$–0.33 in AM Her and $R_{O3}/R_{O1} < 0.1$ in EF Eri. Future transfer calculations at high density may be used to determine whether these R_{O3}/R_{O1} values are consistent with broadening of He II Lyα.

5.2. *Geometry from Bowen Lines*

In Papers I and II, we used observed values of I_{3133}/I_{3204} to infer a Bowen yield. This yield then provides a constraint on the He II Lyα optical depth (τ_L), which can be coupled with the He II emission measure (from I_{3204}) to solve for the Bowen ELR geometry. This approach assumed that case B recombination applies to the He II line spectrum. However, in AM Her the large values of τ_{1640} (§ 4.3) suggest that case B is invalid. We therefore consider the opposite limit for He II, in which the level populations approach LTE. As a consistency check on the LTE assumption, we show later that, at the lower end of the range of derived temperatures, He II $\lambda 1640$ is collisionally de-excited; at the higher end, approximate collisional equilibrium between the $n = 2$ and $n = 3$ levels is maintained. Levels that produce higher series lines (e.g., $\lambda 4686$) appear to be nearly in collisional equilibrium through the entire range of temperatures. In LTE, the intensity of He II Lyα is given by $B(\nu, T)$ at the frequency corresponding to line center and the intrinsic electron temperature. The rate of pumping the O III $2p3d\,^3P_2^o$ state (O1 process) is given by $b_{2p^2,2p3d}\,B_{304}(T)$, where b is the Einstein b coefficient, and $B_{304}(T) = B[(\nu = c/304\ \text{Å}), T]$. We follow the convention for Einstein coefficients used in Rybicki & Lightman (1979), in which the units of b are ergs^{-1} cm^2 s^{-1}. Therefore, we may write for the observed $\lambda 3133$ intensity

$$I_{3133} = \frac{b_{2p^2,2p3d}\,B_{304}(T)(h\nu)_{3133}\,n_{\rm O\,III}\,\frac{4}{3}\pi R^3}{4\pi D^2}\ \text{ergs cm}^{-2}\ \text{s}^{-1}, \tag{7}$$

where R is the Bowen ELR size and D is the distance to the source. We now require the values of $n_{\rm O\,III}/n_{\rm He\,II}$, $n_{\rm He\,II}/n_{\rm H\,II}$, and $n_e/n_{\rm H\,II}$ at the He III front, the likely site of production of the Bowen lines. The value of $n_{\rm O\,III}/n_{\rm He\,II}$ is close to the solar element abundance ratio O/He ($= 8.3 \times 10^{-3}$) in Model 5 of Kallman & McCray (1982), a photoionization calculation where the underlying spectrum consists of both hard and soft X-ray components. The soft X-ray component—a 30,000 K blackbody—is somewhat weaker than the observed soft X-ray contribution in the spectra of several known AM Hers (Beuermann 1988), so that the value of $n_{\rm O\,III}/n_{\rm He\,II}$ is only approximate. We adopt the solar abundance ratio He/H, i.e., $n_{\rm He\,II}/n_{\rm H\,II} = 0.1$ for the ionic ratio of He II to H II. At the He III front, most of the hydrogen is ionized. To specify the electron density, we assume that only helium and hydrogen species contribute to n_e. Assuming $n_{\rm He\,II} = n_{\rm He\,III}$, as expected near the He III front, yields $n_e = 1.3 n_{\rm H\,II}$.

A second equation involving n_e and R is given by the values of line-center optical depth in He II $\lambda 1640$ derived in § 4. We have

$$\tau_{1640} = n_{\rm He\,II,2}\,\sigma_{23}\,R, \tag{8}$$

where $n_{\rm He\,II,2}$ is the density of the excited $n = 2$ state, and σ_{23} is the line-center photoabsorption cross section. In LTE, the excited state density is related to $n_{\rm He\,II}$ essentially by a Boltzmann factor, $\exp(-47.4/T_4)$. This same exponential appears in $B_{304}(T)$. We therefore find

$$I_{13} = 3.03 \times 10^{14} \exp(-47.4/T_4) n_{13} R_{11}^3 d_{75}^{-2}, \tag{9a}$$

and

$$\tau_{1640} = 5.16 \times 10^{10} n_{13} R_{11} \exp(-47.4/T_4) T_4^{-1/2}, \tag{9b}$$

where $I_{13} = I_{3133}/10^{-13}$ ergs cm^{-2} s^{-1}, $n_{13} = n_e/(10^{13}\ \text{cm}^{-3})$, $R_{11} = R/(10^{11}\ \text{cm})$, and $d_{75} = D/(75\ \text{pc})$. Note that we have used Wien's law to evaluate the blackbody function, an approximation valid over the relevant range of temperatures. The preceding set of equations can be solved to find

$$n_{13} = 2.20 \times 10^{-9} \tau_{1640}^{3/2} x_{e10}^{3/2} T_4^{3/4} \exp(47.4/T_4) d_{75}^{-1} I_{13}^{-1/2}, \tag{10a}$$

and

$$R_{11} = 0.011 d_{75} I_{13}^{1/2} \tau_{1640}^{-1/2} T_4^{-1/4} x_{O3}^{-1/2}. \tag{10b}$$

These expressions can now be used to set limits on the size and density of the Bowen ELR in AM Her and EF Eri. The largest uncertainty in our determination of these quantities is the exponential temperature dependence in the equation for n_{13}. In § 4.3, we found that in AM Her the values of T_4 and τ_{1640} in the He II zone are inversely correlated (approximately). For the lowest allowed temperatures, $T_4 \gtrsim 2$, the calculations gave $\tau_{1640} \approx 200$. The analysis of § 4 unfortunately does not provide a useful upper limit to the temperature over the range $2 < T_4 < 9$. However, we expect that $T_4 \approx 2$–3.8, and hence $\tau_{1640} \approx 200$–13, in the He II zone. Model 5 of Kallman & McCray (1982) gives $T_4 \approx 2$. Also, for $T_4 = 3.8$, we get $n_{13} = 2.7 \times 10^{-2}$. This value represents the critical density for collisional de-excitation of N IV] $\lambda 1488$, a line undetected in the *IUE* spectrum of AM Her (Heise & Verbunt 1988). In the He II zone, the N IV ion is expected to be present (Kallman & McCray 1982).

For AM Her, we take $d_{75} = 1$, in accordance with Young & Schneider (1979) and take $I_{13} = 7.6$, an orbit-averaged value from our data. The set of acceptable solutions for n_{13} and R_{11} is given in Figure 10. Each point is labeled by the corresponding value of T_4. Typical error bars, reflecting the uncertainty in determining τ_{1640} from our confidence figures (Fig. 9), are shown. We find $8.59 \times 10^4 > n_{13} > 2.7 \times 10^{-2}$ and $6.26 \times 10^{-3} < R_{11} < 1.79 \times 10^{-2}$, when the limits correspond to $T_4 = 2$ and $T_4 = 3.8$, respectively. The large range of densities reflects the strong temperature dependence in the expression for n_{13}; better estimates of T_4 available from future observations would help to tighten the constraints. The LTE assumption can be shown to be consistent for these parameters. Over the range $T_4 \approx 2$–2.9, the 1640 Å line is collisionally de-excited; also, for $T_4 \gtrsim 2.9$, the collisional excitation rate of the $3d$ level is significant compared with the de-excitation rate ($\gtrsim 8\%$). The system is therefore driven toward LTE. Higher H II levels go readily to LTE.

For $T_4 \lesssim 2.8$, our calculated densities are larger than n_e

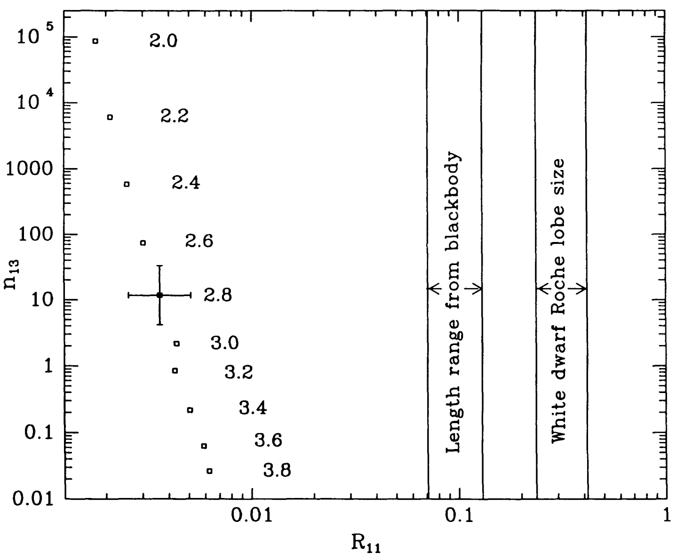

FIG. 10.—Size and electron limits for AM Her. Possible solutions for n_{13} ($=n_e/10^{13}$ cm^{-3}) and R_{11} ($=R/10^{11}$ cm) from the discussion of § 5.2 are shown. They are indicated with squares, with temperature in units of 10^4 K at right. Typical error bars, which reflect uncertainty in the determination of τ_{1640} (see Fig. 9), are shown. We also show the length scale predicted by the flux in optically thick He II λ4686. In addition, we show the range of acceptable sizes of the white dwarf Roche lobe obtained by Young & Schneider (1979).

values in the H I zone obtained by S77, $n_e \approx (1\text{–}20) \times 10^{13}$ cm^{-3}. Also, the derived physical size for the Bowen ELR is significantly less than the radius of the white dwarf's Roche lobe as constrained by Young & Schneider (1979): (0.24–0.42) $\times 10^{11}$ cm (Fig. 10). This suggests that we may be probing a length scale of the accretion column, which some have proposed as the source of line emission in AM Her (e.g., Stockman 1988).

An estimate of the projected area of the ELR is provided by the observed value of I_{4686}. The flux of an optically thick line is given by $(A_{em}/D^2) \int B(\nu, T) [1 - \exp(-\tau_\nu)] d\nu$, where A_{em} is the emitting area. We use the confidence regions for τ_{1640} and T together with observed He II fluxes to calculate area values. This approach gives $A_{em} \approx (1.4\text{–}5.0) \times 10^{20}$ cm^{+2}, where the limiting values correspond to $T_4 = 3.8$ and $T_4 = 2$, respectively. The corresponding range of sizes, in units of 10^{11} cm, is $\sim$0.07–0.13, which is significantly higher than the derived Bowen ELR size (Fig. 10). These results suggest that the assumption of a spherical ELR in AM Her may be too simplistic. This may not be surprising if the accretion column is, in fact, the ELR. In that case, the geometry would be cylindrical with a radius at least several times smaller than its length. We might expect substantial variation in the Bowen and He II line intensities as the orientation of our line of sight with respect to the cylinder changes over the course of the binary orbit. As indicated in § 2.2, our data do exhibit such variations; however, further observations are required to constrain models of this type more fully.

In the case of EF Eri, the limited data do not permit a determination of τ_{1640} and T (§ 4). However, we may formally solve equations (10) using opacity and temperature values from AM Her. From Young & Schneider (1981), we adopt $d_{75} = 2$, corresponding to a spectral type M4.5 V for the secondary. We find $1.30 \times 10^{-2} < n_{13} < 9.67 \times 10^4$ and $5.97 \times 10^{-3} > R_{11} > 1.59 \times 10^{-3}$, where the endpoints are for $T_4 = 3.8$ and $T_4 = 2.0$, respectively. Our derived values of R_{11} can be compared to the size of the Roche lobe of the primary, (0.40–0.50) $\times 10^{11}$ cm, which is well constrained for a wide range of values of the white dwarf mass (0.3–1.4 $M_\odot$). Hence, the derived upper limits to the ELR length scale are significantly smaller than the Roche lobe size. The results are similar to those derived for AM Her.

Other AM Her systems studied in the near-UV spectral region may also show strong Bowen fluorescence emission. We suggest that future observations of the Bowen lines be performed, particularly on those systems for which some details of the accretion geometry are known. The Bowen lines may also be an important diagnostic aid to the AM Her systems which will be newly discovered by upcoming X-ray and extreme UV missions.

This research was supported by grants from the California Space Institute, the Institute for Geophysics and Planetary Physics at Lawrence Livermore National Laboratory, the National Science Foundation, and the NASA Innovative Research Fund. For one of us (J. S.) this represents the third and final scientific chapter of a PhD dissertation. We thank Moshe Elitzur, Chris Mauche, Chris McKee, David Neufeld, and John Raymond for useful discussions. Help with the observations was provided by the day and night assistants at Lick Observatory, which is partly supported by NSF Core Bock grant 86-14510 to the University of California.

REFERENCES

Aller, L. H., Bowen, I. S., & Wilson, O. L. 1963, ApJ, 138, 1013
Beuermann, K. 1988, Adv. Space Res., 8 (2), 283
Bowen, I. S. 1934, PASP, 84, 68
Brocklehurst, M. 1972, MNRAS, 157, 211
Crampton, D., & Cowley, A. P. 1977, PASP, 89, 374
Cropper, M. 1988, Adv. Space Res., 8 (2), 273
Deguchi, S. 1985, ApJ, 291, 492; erratum 303, 901 (1986)
Elitzur, M. E., Ferland, G. J., Mathews, W. G., & Shields, G. A. 1983, ApJ, 272, L55
Green, R. F., Ferguson, D. H., Liebert, J., & Schmidt, M. 1982, PASP, 94, 560
Greenstein, J. L., Sargent, W. L. W., Boroson, T. A., & Boksenberg, A. 1977, ApJ, 218 L121
Harrington, J. P. 1972, ApJ, 176, 127
Heise, J., & Verbunt, F. 1988, A&A, 189, 112
Hummer, D. G., & Storey, P. J. 1987, MNRAS, 224, 801
Kallman, T. R., & McCray, R. 1980, ApJ, 242, 615 (KM80)
———. 1982, ApJS, 50, 263
Kastner, S. O., Behring, W. E., & Bhatia, A. K. 1983, ApJS, 53, 129
Kastner, S. O., & Bhatia, A. K. 1990, ApJ, 362, 745
Lampton, M., Margon, B., & Bowyer, S. 1976, ApJ, 208, 177
McCarthy, P., Bowyer, S., & Clarke, J. T. 1986, ApJ, 311, 873
McClintock, J. E., Canizares, C. R., & Tarter, B. E. 1975, ApJ, 198, 641
Miller, J. S., & Stone, R. P. S. 1987, Lick. Obs. Tech. Rept. No. 48
Neufeld, D. A. 1990a, ApJ, 350, 216
———. 1990b, private communication
Oke, J. B., & Gunn, J. E. 1983, ApJ, 266, 713
Osterbrock, D. E. 1989, Astrophysics of Gaseous Nebulae and Active Galactic Nuclei (2d ed.; Mill Valley: University Science Books)
Osterbrock, D. E., & Wallace, R. K. 1977, Ap. Letters, 19, 11
Patterson, J., Williams, G., & Hiltner, W. A. 1981, ApJ, 245, 618
Raymond, J. 1989, private communication
Raymond, J. C., Black, J. H., Dupree, A. K., Gursky, H., Hartmann, L., & Matilsky, T. A. 1979, ApJ, 230, L95
Rosen, S. R., Mason, K. O., & Córdova, F. A. 1987, MNRAS, 224, 287
Rybicki, G. B., & Lightman, A. P. 1979, Radiative Processes in Astrophysics (New York: Wiley)
Saraph, H. E., & Seaton, M. J. 1980, MNRAS, 193, 617 (SS)
Schachter, J., Filippenko, A. V., & Kahn, S. M. 1989, ApJ, 340, 1049; erratum, 362, 379 (1990) (Paper I)
———. 1990, ApJ, 362, 74 (Paper II)
Schmidt, G. D., Stockman, H. S., & Grandi, S. A. 1986, ApJ, 300, 804
Schneider, D. P., & Young, P. 1980, ApJ, 240, 871

Stockman, H. S. 1988, in Polarized Radiation of Circumstellar Origin, ed. G. V. Coyne, A. M. Magalhaes, A. F. J. Moffat, R. E. Schulte-Ladbeck, S. Tapia, & D. T. Wickramasinghe (Vatican City: Vatican Observatory), p. 237
Stockman, H. S., Schmidt, G. D., Angel, J. R. P., Liebert, J., Tapia, S., & Beaver, E. A. 1977, ApJ, 217, 815 (S77)
Taylor, P. O., & Dunn, G. H. 1973, Phys. Rev. A., 8, 2304
Tuohy, I. R., Mason, K. O., Garmire, G. P., & Lamb, F. K. 1981, ApJ, 245, 183
White, N. E. 1981, ApJ, 244, L85
Williams, R. E., Woolf, N. J., Hege, E. K., Moore, R. L., & Kopriva, D. A. 1978, ApJ, 224, 171
Young, P., & Schneider, D. P. 1979, ApJ, 230, 502
———. 1981, ApJ, 247, 960
Young, P., Schneider, D. P., Sargent, W. L. W., & Boksenberg, A. 1982, ApJ, 252, 269